



Patni, M., Minera Rebullá, S., Groh, R., Pirrera, A., & Weaver, P. (2019). On the accuracy of localised 3D stress fields in tow-steered laminated composite structures. *Composite Structures*, 225, [111034]. <https://doi.org/10.1016/j.compstruct.2019.111034>

Peer reviewed version

License (if available):
CC BY-NC-ND

Link to published version (if available):
[10.1016/j.compstruct.2019.111034](https://doi.org/10.1016/j.compstruct.2019.111034)

[Link to publication record in Explore Bristol Research](#)
PDF-document

This is the author accepted manuscript (AAM). The final published version (version of record) is available online via Elsevier at <https://www.sciencedirect.com/science/article/pii/S0263822319303630>. Please refer to any applicable terms of use of the publisher.

University of Bristol - Explore Bristol Research

General rights

This document is made available in accordance with publisher policies. Please cite only the published version using the reference above. Full terms of use are available: <http://www.bristol.ac.uk/red/research-policy/pure/user-guides/ebr-terms/>

On the accuracy of localised 3D stress fields in tow-steered laminated composite structures

M. Patni^{a,*}, S. Minera^a, R.M.J. Groh^a, A. Pirrera^a, P.M. Weaver^{a,b,*}

^a*Bristol Composites Institute (ACCIS), Department of Aerospace Engineering, University of Bristol, Queen's Building, University Walk, Bristol BS8 1TR, UK.*

^b*Bernal Institute, School of Engineering, University of Limerick, Castletroy, Ireland.*

Abstract

Variable Angle Tow (VAT) composites offer increased freedom for tailoring material properties compared to traditional straight-fibre composites. This increased freedom leads to greater design flexibility for enhanced structural performance but comes at the cost of more complex, spatially-varying displacement, strain and stress fields. To maximise the utility of VAT composites, a computationally efficient, yet accurate, numerical framework is needed. To this end, we employ a modelling approach that builds upon the recently developed, hierarchical Serendipity Lagrange finite elements. Three-dimensional (3D) stress distribution is obtained using the present modelling technique and verified against 3D finite element solutions, as well as other formulations available in the literature. A key advantage of the present approach is the ability to predict accurate 3D stress fields efficiently, *i.e.* with reduced computational effort, including around local features such as geometric, kinematic or constitutive boundaries. Moreover, the present work concerns the peculiarities of commonly used mathematical expressions for describing spatially varying fibre orientations across VAT laminates. The presence of an absolute value in the function used to describe fibre orientation can lead to discontinuities in fibre angle slope and curvature. In turn, these discontinuities lead to mathematical singularities in the constitutive relations along the laminate. If this singularity is not appropriately modelled as a boundary of the continuum, but rather as an interior point of the continuum, stresses may be predicted inaccurately. Compared to other models in the literature, our method is capable of unveiling detailed 3D stresses readily and accurately also in the vicinity of this singularity.

Keywords: Variable angle tow composites; 3D stress fields; Unified Formulation

1. Introduction

Over the last few decades, the application of laminated composite materials has significantly increased in various engineering disciplines. This increase is due mainly to their high specific strength and stiffness, good fatigue resistance and damage tolerance characteristics. Continuous fibre-reinforced composites allow designers to tailor the material properties through the thickness of a laminate by varying the fibre orientation of each ply and optimising the stacking sequence for structural performance. The concept of steering fibres (tows) curvilinearly within individual laminae adds a further dimension to the tailoring capability and can improve structural performance without increasing weight. Hence, studies on so-called Variable Angle Tow (VAT) composites are gaining attention. VAT composites are also referred to as variable-stiffness composites [1], curvilinear fibre-reinforced composites [2] or variable-axial fiber-reinforced composites [3] in the literature.

The notion of tailoring the structural performance by steering the fibre paths spatially in the plane of a composite laminate has been proposed in the early 1970s [4]. However, recent advancements in composite

*Corresponding authors: mayank.patni@bristol.ac.uk, paul.weaver@bristol.ac.uk

manufacturing technologies have facilitated the production of laminates with variable angle tows and this has spawned an increased interest in the topic. Compared to constant-stiffness laminates (straight fibre path), superior structural performance can be achieved for variable-stiffness laminates, where the in-plane stiffness varies spatially throughout the structure [5–8]. Previous works on VAT laminates have extensively demonstrated significant improvements in the stress distribution around holes [9, 10]. Hyer and Lee [7] studied variable stiffness composites with circular holes, by varying the fibre orientations on a region-by-region basis. Stress redistributions driven by tow-steering have been shown to substantially improve the compressive buckling limit of flat laminates [11, 12]. Wu *et al.* [12–14] solved the pre-buckling, buckling and initial post-buckling problems of flat VAT plates and developed a two-step optimisation framework to minimise the end-shortening strain in the post-buckling regime for a fixed compressive load. Hao *et al.* [15] proposed a bi-level optimisation framework to find the optimum design of variable-stiffness panels with multiple cutouts. On a component level, Stodieck *et al.* [16] have shown tow-steered laminates improve the aeroelastic behaviour of rectangular composite wings when compared to unidirectional laminates. Coburn *et al.* [17] proposed a semi-analytical method for the buckling analysis of blade-stiffened VAT panels and investigated the concept of using VAT to obtain greater buckling loads. Recently, Scott *et al.* [18] have shown variable stiffness blades improve the performance characteristics of wind turbine systems.

To date, most studies on VAT composites deal with global structural phenomena, *e.g.* vibration and buckling [7, 8, 19–23]. For an extensive review of the literature, the interested reader is referred to [24]. With the increasing promise of VAT composites for structural design, there is also a need for developing accurate, yet computationally efficient, modelling techniques for predicting 3D stress fields. In general, predicting 3D stress fields accurately in composite structures is important as through-thickness damage, such as delaminations, is driven by transverse shear and transverse normal stresses. In VAT composites there are additional complexities because variations in material properties can lead to non-intuitive and complex stress variations increasing the possibility of damage [25]. In addition, even though buckling is a global structural phenomenon, increases in the buckling load using variable fibre paths occur as a result of local stress redistributions. Capturing localised, three-dimensional stress fields accurately is therefore essential for safe design. However, relatively little work has been conducted in this direction. Whilst investigating VAT plates Akbarzadeh *et al.* [26] examined the effect of transverse shear deformation and embedded manufacturing defects on the structural responses. Akhavan and Ribeiro [27, 28] used a p-version finite element (FE) approach based on a Reddy-type third-order shear deformation theory to investigate the natural modes of vibration, the non-linear bending deflection, and the stresses. Díaz *et al.* [29] presented a numerical method for obtaining the interlaminar stresses in variable stiffness composite panels. Later, Groh and Weaver [30] showed that using Reddy-type models can lead to static inconsistencies at clamped boundaries. Recently, Soriano and Díaz [31] carried out three-dimensional FE analyses and introduced a continuum damage mechanics model to study their failure processes.

Most papers published on modelling VAT laminates use finely meshed FE models that can be computationally prohibitive for rapid design iterations. In this regard, several attempts have been made to develop computationally more efficient numerical models. Demasi *et al.* [32] formulated equivalent single-layer, zig-zag and layer-wise models based on the Generalised Unified Formulation (GUF) [33] and benchmarked the performance of the different approaches. However, the study mainly focused on highlighting the computational efficiency gains over 3D FE models. By validating relatively simple stacking sequences, the robustness of the approach in analysing arbitrary and complex lay-ups remains an open question. Tornabene *et al.* [34, 35] developed a structural model based on an equivalent single-layer approach for free vibration and linear static analysis of doubly-curved shells reinforced by curvilinear fibres. The Generalized Differential Quadrature (GDQ) method is employed to obtain the numerical solution. Groh and Weaver [36, 37] described a third-order zig-zag implementation within a Hellinger-Reissner mixed variational framework and use it to predict accurate 3D stresses for arbitrary VAT laminates. However, they observed discrepancies in the transverse normal stresses for some laminates when compared with 3D FE solutions. Resolving this disparity in transverse stress results is one of the motivations of the present study. Moreover, an important aspect of the present work, in contrast to published articles on VAT composites, is highlighting the effect of mathematical singularities present in the constitutive relations along the laminate. The presence of an absolute function in the fibre orientation distribution leads to discontinuities and is widely employed by

many researchers. However, to the authors' knowledge, none of them discuss its implications on stress computation. Negative implications would arise if this singularity is not appropriately modelled. For instance, this could happen by employing the Differential Quadrature Method (DQM) whilst also modelling the VAT composite beam structure using a single continuous domain [38]. Furthermore, inaccuracies in transverse stress fields could arise if these stress fields are computed by employing a stress recovery technique (using Cauchy's 3D equilibrium equations) as adopted by Díaz *et al.* [29].

The present work extends the authors' work on predicting localised 3D stress fields in laminated composite and sandwich structures [39] to the analysis of tow-steered composite structures. To model VAT beam- and plate-like 3D structures, we use finite elements based on Serendipity Lagrange expansions (SLE) within the Unified Formulation framework developed by Carrera and co-workers [40–42]. Serendipity Lagrange elements solve some of the shortcomings of the most commonly used Unified Formulation beam models based on Taylor and Lagrange expansion functions. For Taylor models, as the order of expansion increases, the conditioning number of the stiffness matrix decreases exponentially. This problem makes the system ill-conditioned and numerically unstable. SLE elements overcome this limitation and are therefore suitable for analysing beams with complex cross-sections. Similarly to Lagrange expansion models, SLE elements allow for cross-sectional discretisation, and therefore, are particularly suited for capturing localised stress fields near boundaries, discontinuities and points of load application. Cross-sections are also discretised in the Lagrange model; model building, however, is cumbersome because re-meshing is the only way to improve accuracy. A layer-wise approach is adopted and, together with the properties of the SLE model, *i.e.* refinement by combined cross-sectional discretisation and hierarchical expansion, both local and global responses are obtained accurately and is done so in a computationally efficient manner. As the formulation is displacement-based, it does not ensure continuous transverse stresses across layer interfaces. An extra post-processing step is generally required to derive these stresses accurately from displacement variables. In some cases, however, the model fidelity proves to be sufficient. Therefore, in the present work, transverse stresses are computed directly using the constitutive equations, unless specified otherwise.

The remainder of the paper is structured as follows. Section 2 provides an overview of the Unified Formulation framework based on the Serendipity Lagrange expansion finite elements. In Section 3, the model for VAT beam- and plate-like structures is verified against 3D FE models in a linear static setting. The results obtained are also compared with a mixed formulation approach available in the literature [36]. Finally, conclusions are drawn in Section 4.

2. Formulation

2.1. Preliminaries

Consider a variable angle tow laminated beam of length L , rectangular cross-section of width b and thickness h , composed of N layers. The material properties and the thickness of each layer may be entirely different. The beam is referred to in a Cartesian coordinate system (x, y, z) , where the y -direction is defined to be along the principle beam axis, while the z -axis is in the transverse stacking direction as shown in Figure 1. Let θ denote the fibre angle measured with respect to the y direction and varying along the beam's span. Finally, let the superscript k be used to refer to layer k .

2.2. Finite Element Formulation based on Serendipity Lagrange Expansions

Our model employs the Unified Formulation framework, where a 3D structure is discretised with a finite number of transverse planes running along the longitudinal axis of the structure as shown in Figure 2a. For simplicity, the structure's longitudinal axis can be thought of as a beam and the transverse planes as its cross-sections. The Unified Formulation [40, 43] relies on a displacement-based version of the finite element method. The advantage of a finite element discretisation is that arbitrary geometries and boundary conditions can readily be modelled. In the current setting, the longitudinal axis of the structure is discretised

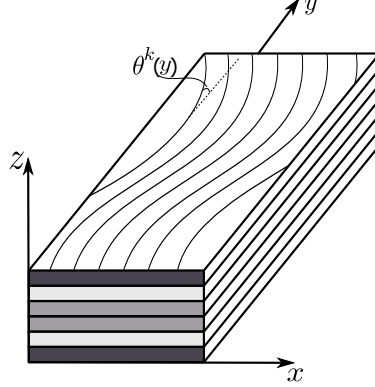


Figure 1: Reference system for a VAT laminated beam.

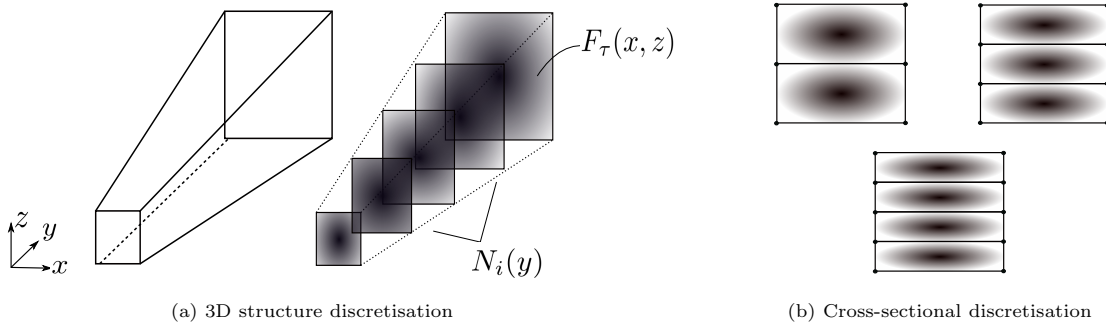


Figure 2: Serendipity Lagrange element based Unified Formulation framework

with N_e -noded, traditional 1D finite elements, so that the displacement field can be approximated element-wise by means of local shape functions $N_i(y)$, and generalised nodal displacements, $\mathbf{u}_i(x, z)$, such that

$$\mathbf{u}(x, y, z) = \sum_{i=1}^{N_e} N_i(y) \mathbf{u}_i(x, z). \quad (1)$$

The transverse, or cross-sectional deformations, are approximated using hierarchical Serendipity Lagrange expansion (SLE) functions $F_\tau(x, z)$ [44]. Adopting this expansion model, cross-sections are further discretised using four-noded Lagrange sub-domains (SLE nodes) and the displacement field within sub-domains can be enriched by increasing the order of the local Serendipity Lagrange expansion. The cross-sectional displacement field at the i^{th} beam node is expressed as

$$\mathbf{u}_i(x, z) = \sum_{\tau=1}^m F_\tau(x, z) \mathbf{u}_{i\tau}, \quad (2)$$

where τ is the discretisation variable, m is the number of terms depending on the order of SL expansion, and $\mathbf{u}_{i\tau}$ are generalized three-dimensional displacement vectors. This model allows a layer-wise approach to be implemented directly by using a sub-domain for each layer and where the kinematics within each layer (or sub-domain) can be varied hierarchically as depicted in Figure 2b (where the shading denotes hierarchical functions spanning the sub-domain). The number of degrees of freedom per SL finite element depends on the order of expansion. The reader is referred to [44] for a more detailed implementation and treatment of SLE models.

By introducing the cross-sectional approximation of Eq. (2) into the FE discretisation along the beam axis of Eq. (1), the displacement field reads

$$\mathbf{u}(x, y, z) = \sum_{i=1}^{N_e} \sum_{\tau=1}^m N_i(y) F_\tau(x, z) \mathbf{u}_{i\tau}. \quad (3)$$

For the sake of clarity, it is important to stress that, using Eq. (3), the cross-sectional mesh captures the warping of the cross-section with one set of 2D shape functions ($F_\tau(x, z)$), while the axial behaviour is modelled by a separate 1D mesh (indicated by discretisation variable i) with an independent set of 1D shape functions ($N_i(y)$). This approach differentiates the method from classic 3D FEM, where 3D shape functions are used over volumetric brick or tetrahedral elements that offer no separation of cross-sectional and axial deformations. Moreover, the current methodology overcomes the limitation on the aspect ratio of a 3D brick element in FE analysis by decoupling the shape functions along the longitudinal axis and across the transverse plane.

Elastic equilibrium is enforced via the Principle of Virtual Displacements, by equating the internal and external virtual work, δW_{int} and δW_{ext} . By definition, the internal work is the work done by the internal stresses over the corresponding internal strains and is equivalent to the elastic strain energy. Noting that $W_{\text{int}} = \sum_e W_{\text{int}}^e$, where W_{int}^e represents the strain energy per element, letting l_e be the length of the generic beam element, and A the cross-sectional area

$$\delta W_{\text{int}}^e = \int_{l_e} \int_A \delta \boldsymbol{\varepsilon}^\top \boldsymbol{\sigma} dA dl. \quad (4)$$

In the notation of the Unified Formulation, the internal work can be re-written as

$$\delta W_{\text{int}}^e = \delta \mathbf{u}_{sj}^\top \mathbf{K}_e^{\tau sij} \mathbf{u}_{\tau i}, \quad (5)$$

where the term $\mathbf{K}_e^{\tau sij}$ is referred to as the elemental *Fundamental Nucleus*. Its explicit form for VAT composites can be found in Appendix A. Fundamental nuclei are assembled into a global stiffness matrix following the standard finite element procedure. For the sake of brevity, the derivation of the fundamental nucleus of the loading vector from the virtual variation of the external work is not reported here, but can be found in [43].

2.3. Strain and Stress Components

From basic elasticity, the generalised strain component vector can be written as

$$\boldsymbol{\varepsilon} = \mathcal{D} \mathbf{u}, \quad (6)$$

where $\boldsymbol{\varepsilon}^\top = \{\varepsilon_{xx}, \varepsilon_{yy}, \varepsilon_{zz}, \gamma_{yz}, \gamma_{zx}, \gamma_{xy}\}$ and \mathcal{D} is the kinematic partial differential operator

$$\mathcal{D} = \begin{bmatrix} \frac{\partial}{\partial x} & 0 & 0 \\ 0 & \frac{\partial}{\partial y} & 0 \\ 0 & 0 & \frac{\partial}{\partial z} \\ 0 & \frac{\partial}{\partial z} & \frac{\partial}{\partial y} \\ \frac{\partial}{\partial z} & 0 & \frac{\partial}{\partial x} \\ \frac{\partial}{\partial y} & \frac{\partial}{\partial x} & 0 \end{bmatrix}. \quad (7)$$

The laminates considered in this study are assumed to be homogeneous and operate in the linear elastic range. Layerwise stresses are usually computed using the constitutive relation, $\boldsymbol{\sigma}^k = \bar{\mathbf{C}}^k \boldsymbol{\varepsilon}^k$, where $\bar{\mathbf{C}}^k$ is the transformed material stiffness matrix depending on the mechanical properties of the material and on fibre angle. However, if the modelling fidelity is not sufficient most displacement-based approaches produce discontinuous transverse stresses at the layer interfaces, which violates the traction equilibrium condition between layers. In order to improve the 3D stress fields predicted by displacement-based models, transverse

stresses can be recovered by employing the indefinite equilibrium equations of 3D elasticity and integrating in-plane stresses in the thickness direction. The 3D stress equilibrium equations for the static case, and in the absence of body forces, are

$$\sigma_{ij,j} = 0, \quad i, j = x, y, z, \quad (8)$$

where a comma denotes differentiation and Einstein's summation notation has been used. In summary, the in-plane stresses, σ_{xx} , σ_{yy} and τ_{xy} , are computed conventionally using the constitutive relations. Transverse shear and normal stresses, τ_{xz} , τ_{yz} , and σ_{zz} are calculated as

$$\sigma_{iz}^k(z) = \sigma_{iz_b}^k - \int_{z_b^k}^z (\sigma_{ix,x} + \sigma_{iy,y}) dz, \quad (9)$$

where $\sigma_{iz}^k(z)$ is the stress value in the k^{th} -layer and $\sigma_{iz_b}^k$ is the stress value at the bottom of the k^{th} -layer.

3. Numerical Results and Discussion

With the aim of assessing the accuracy and robustness of the SLE-based Unified Formulation in analysing VAT structures, static analysis results of VAT composite beam- and plate-like structures are presented in this section. Results obtained using the present approach are validated with 3D FE solutions and are compared with a mixed displacement/stress-based, third-order zig-zag theory available in the literature [36]. In this work, VAT composite structures with linear fibre angle variation along one direction and constant stiffness properties in the orthogonal direction are considered. The angle variation along the spanwise direction, y , of each ply, k , is defined using the notation given by Gürdal and Olmedo [1],

$$\theta^{(k)}(y) = \frac{2(T_1^{(k)} - T_0^{(k)})}{L} \left| y - \frac{L}{2} \right| + T_0^{(k)}, \quad (10)$$

where $\theta^{(k)}(y)$ is the local fibre angle at y , and $T_0^{(k)}$ and $T_1^{(k)}$, written as $\langle T_0^{(k)} | T_1^{(k)} \rangle$, are the fibre angles at the beam midspan $y = L/2$ and ends $y = 0, L$, respectively. Hence, the fibre angle in each ply takes the value $T_1^{(k)}$ at one end of the beam, being steered to $T_0^{(k)}$ at the mid-span, and returning to $T_1^{(k)}$ at the other end. Due to the variable-stiffness design of the curvilinear tow paths, the material stiffness tensor \mathbf{C} is a function of the y -location.

The material properties and stacking sequences modelled in this section are shown in Tables 1 and 2, respectively. Materials p, pvc, h represent an orthotropic carbon-fibre reinforced plastic, isotropic poly-vinyl chloride foam, and transversely isotropic honey-comb core, respectively. IM7 stands for IM7 8852, a carbon-fibre reinforced plastic material commonly used in industry. In most of the laminates considered herein, the variation in fibre angle along the length of the beam is 90° , which is greater than the manufacturing capability of most tow-steering machines. However, this extreme case of stiffness variation along the beam length provides a good test case for model verification.

3.1. Tow-Steered Composite Beam-like Structure

A multilayered beam-like 3D structure with length-to-thickness ratio $L/h = 10$, comprising N_l VAT composite layers is considered in the present study. The beam, aligned with the Cartesian y -axis, is clamped at both ends, $y = 0$ and $y = L$, and is assumed to undergo static deformations in plane strain (x -direction), under a uniformly distributed load equally divided between the top and the bottom surfaces $P_z^t = P_z^b = -q_0/2$, as shown in Figure 3. To test the general applicability of the Unified Formulation based on the Serendipity Lagrange expansion functions (UF-SLE), a variety of symmetric and non-symmetric VAT composite beams are analysed. These laminates are defined by items A-J in Table 2, where VAT beams A-D are symmetric, E-F are non-symmetric, G-H are symmetric sandwich construction with variable stiffness face layers, and I-J are non-symmetric sandwich construction with hybrid constant-stiffness/variable-stiffness face layers.

In our UF-SLE models, the structures are discretised with 40 B4 (four-noded 1D Lagrange) elements along their length. The cross-sections are divided into sub-domains (one per layer). Within each sub-domain

Table 1: Mechanical properties of the materials considered in the present study. Materials p, pvc, h and IM7 stands for carbon-fibre reinforced plastic, poly-vinyl chloride foam, honeycomb and IM7/8552 composite, respectively.

Material	E_x	E_y	E_z	G_{yz}	G_{xz}	G_{xy}
	[GPa]					
p	6.9	172.37	6.9	3.45	1.38	3.45
pvc	1.723	1.723	1.723	0.663	0.663	0.663
h	1.723×10^{-3}	1.723×10^{-3}	17.23×10^{-3}	6.03×10^{-3}	12.06×10^{-3}	6.9×10^{-6}
IM7	12.0	163.0	12.0	4.0	3.2	5.0
	ν_{yz}		ν_{xz}		ν_{xy}	
p	0.25		0.25		0.01	
pvc	0.3		0.3		0.3	
h	3.0×10^{-5}		3.0×10^{-5}		0.9	
IM7	0.3		0.3		0.022	

Table 2: Stacking sequence for laminates considered in the present study. Subscripts indicate the repetition of a property over the corresponding number of layers.

Laminate	Layer thickness ratio	Material	Stacking sequence
VAT Beam			
A	$[(1/8)_8]$	[IM7 ₈]	$[\langle 90 0 \rangle / \langle -90 0 \rangle / \langle 45 -45 \rangle / \langle -45 45 \rangle]_s$
B	$[(1/8)_8]$	[IM7 ₈]	$[\langle 90 20 \rangle / \langle 45 -25 \rangle / \langle -90 -20 \rangle / \langle -45 25 \rangle]_s$
C	$[(1/3)_3]$	[IM7 ₃]	$[\langle 0 90 \rangle / \langle 90 0 \rangle / \langle 0 90 \rangle]$
D	$[(1/3)_3]$	[IM7 ₃]	$[\langle 90 0 \rangle / \langle 0 90 \rangle / \langle 90 0 \rangle]$
E	$[(1/5)_5]$	[IM7 ₅]	$[\langle 90 30 \rangle / \langle -70 50 \rangle / \langle 60 0 \rangle / \langle -25 35 \rangle / \langle 80 10 \rangle]$
F	$[(1/4)_4]$	[IM7 ₄]	$[\langle 0 70 \rangle / \langle 90 50 \rangle / \langle 20 -40 \rangle / \langle 50 0 \rangle]$
G	$[(1/8)_2/0.5/(1/8)_2]$	[p ₂ /pvc/p ₂]	$[\langle 45 -45 \rangle / \langle -45 45 \rangle / 0 / \langle -45 45 \rangle / \langle 45 -45 \rangle]$
H	$[(1/12)_4/(1/3)/(1/12)_4]$	[p ₄ /pvc/p ₄]	$[\langle 0 90 \rangle / \langle 90 0 \rangle / \langle 0 -90 \rangle / \langle -90 0 \rangle / \dots$ $0 / \langle -90 0 \rangle / \langle 0 -90 \rangle / \langle 90 0 \rangle / \langle 0 90 \rangle]$
I	$[(1/8)_2/0.5/(1/8)_2]$	[p ₂ /pvc/p ₂]	$[\langle 20 -60 \rangle / \langle -20 60 \rangle / 0 / 0 / 90]$
J	$[(1/12)_4/(1/3)/(1/12)_4]$	[p ₄ /pvc/p ₄]	$[\langle 20 -60 \rangle / \langle -20 60 \rangle / \langle 45 -45 \rangle / \langle -45 45 \rangle / \dots$ $0 / 0 / 90 / \langle 35 -35 \rangle / \langle -35 35 \rangle]$
VAT Plate			
K	$[(1/4)_4]$	[IM7 ₄]	$[\langle 0 90 \rangle / \langle 0 -90 \rangle]_s$
L	$[(1/8)_8]$	[IM7 ₈]	$[\langle 0 70 \rangle / \langle 0 -70 \rangle / \langle 90 20 \rangle / \langle -90 -20 \rangle]_s$
M	$[(1/16)_4/0.5/(1/16)_4]$	[IM7 ₄ /h/IM7 ₄]	$[\langle 0 70 \rangle / \langle 0 -70 \rangle / \langle 45 -20 \rangle / \langle -45 20 \rangle / 0 / \dots$ $\langle -45 20 \rangle / \langle 45 -20 \rangle / \langle 0 -70 \rangle / \langle 0 70 \rangle]$

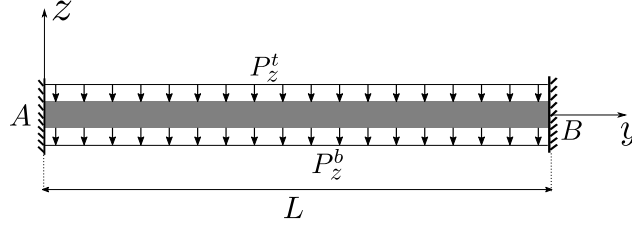


Figure 3: Representation of a multilayered beam-like structure, length-to-thickness ratio $L/h = 10$, clamped at both ends and subjected to a uniformly distributed load over the top and bottom surface.

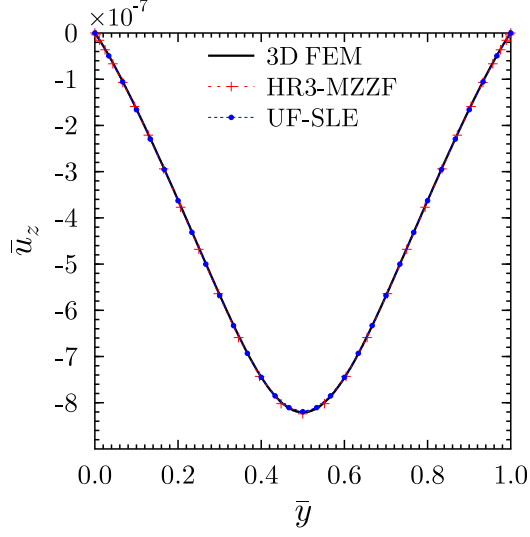
(Serendipity Lagrange element) a fourth-order expansion function is employed (SL4). The number of beam elements and the order of expansion in the cross-section were set through a convergence analysis. For the sake of brevity, only converged results are presented for all cases in the paper. To the authors' knowledge there are no 3D closed-form solutions for VAT composite beams under bending. Therefore, the bending deflection and stress results obtained are compared with a mixed formulation approach based on the Hellinger-Reissner third-order theory [45] with Murakami Zig-Zag function [46] (HR3-MZZF) and 3D FE solutions as given in [36]. It is to be noted that the results available in the literature are based on a plane-strain assumption in the x -direction. Thus, to mimic the plane-strain condition in the present approach, appropriate coupling terms are removed from the material stiffness matrix as described in Appendix B.

Normalised metrics of the bending deflection, u_z , axial stress, σ_{yy} , transverse shear stress, τ_{yz} and transverse normal stress, σ_{zz} , are used for our comparisons as given by

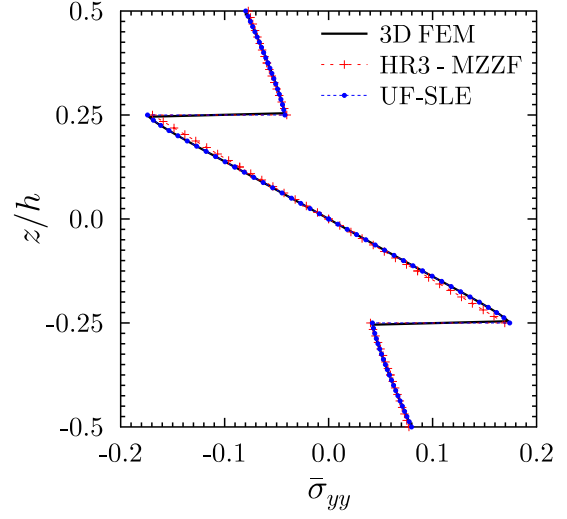
$$\begin{aligned}\bar{u}_z &= \frac{10^6 h^2}{q_0 L^4} \int_{-h/2}^{h/2} u_z(x, y, z), & \bar{\sigma}_{yy} &= \frac{h^2}{q_0 L^2} \cdot \sigma_{yy}(x, y, z), \\ \bar{\tau}_{yz} &= \frac{1}{q_0} \cdot \tau_{yz}(x, y, z), & \bar{\sigma}_{zz} &= \frac{1}{q_0} \cdot \sigma_{zz}(x, y, z).\end{aligned}\tag{11}$$

Figures 4 to 13 show plots of the spanwise bending deflection, \bar{u}_z , through-thickness in-plane stress, $\bar{\sigma}_{yy}$, and transverse normal stress, $\bar{\sigma}_{zz}$, at the mid-span of the beam, and through-thickness transverse shear stress, $\bar{\tau}_{yz}$, at the quarter-span of the beam. From these plots, it is evident that the displacement and stress distributions computed using the UF-SLE model are in an excellent agreement with 3D FE solutions. Furthermore, generally, the UF-SLE model correlates with the 3D FE solutions better than the HR3-MZZF model, particularly for transverse normal stresses, $\bar{\sigma}_{zz}$. Overall, for displacement, \bar{u}_z , axial normal stress, $\bar{\sigma}_{yy}$, and transverse shear stress, $\bar{\tau}_{yz}$, Figures 4 to 9 show a good correlation between 3D FE, HR3-MZZF and UF-SLE models. However, for VAT sandwiches, *i.e.* VAT G, VAT H, VAT I and VAT J, the UF-SLE model (layer-wise approach) is more accurate than the HR3-MZZF model (equivalent single layer approach), due to higher degrees of transverse orthotropy. The greatest differences are observed for the most challenging test case, the non-symmetric sandwich beam VAT J, as shown in Figure 13. These differences are clearly due to the inability of the Murakami's Zig-Zag function (MZZF) to capture the zig-zag effect accurately, when employed for highly heterogeneous sandwich beams. It is noted, however, that the refined zig-zag theory (RZT) introduced by Tessler [47] has been shown to solve this shortcoming and to be capable of predicting the stress response accurately even for highly heterogeneous laminates.

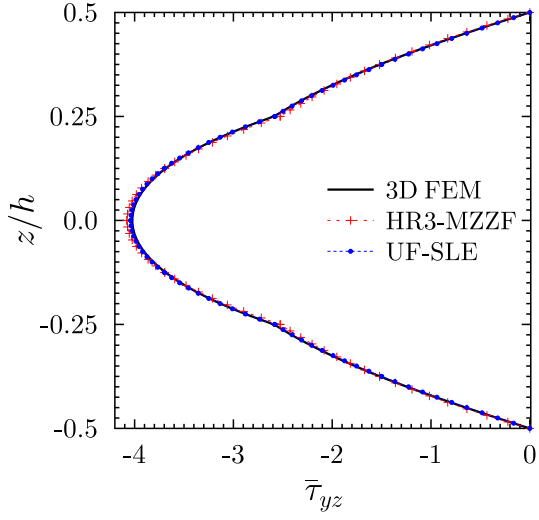
The remainder of this section is focused on: (i) the accuracy of the distributions of through-thickness transverse normal stress, and (ii) a comparison of the 3D FE, HR3-MZZF and UF-SLE, models in term of general accuracy. It is well known that in a displacement-based 3D FE approach, stresses are derived from displacement variables using kinematic and constitutive equations, and therefore, the equilibrium of stresses is only satisfied in a weak (average integral) sense. This means that the residual in the 3D equilibrium equations decreases asymptotically with mesh refinement. In the Hellinger-Reissner (HR) mixed formulation proposed by Groh & Weaver [36], the individual stress assumptions inherently satisfy Cauchy's equilibrium equations. The statement is substantiated in chapter 6 of [36] by computing residuals of Cauchy's equilibrium



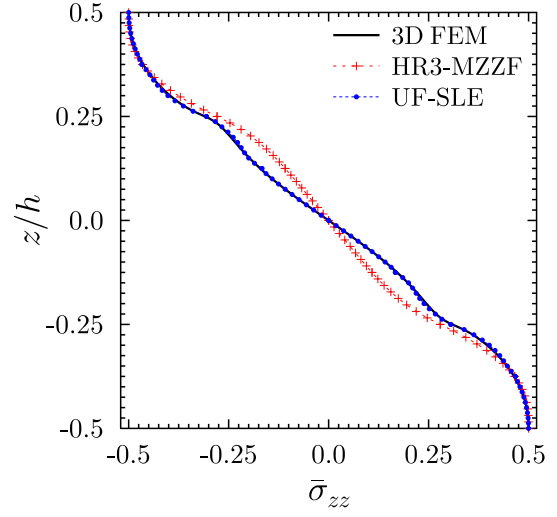
(a) Normalised bending deflection, \bar{u}_z



(b) Axial normal stress, $\bar{\sigma}_{yy}$ at $y = L/2$

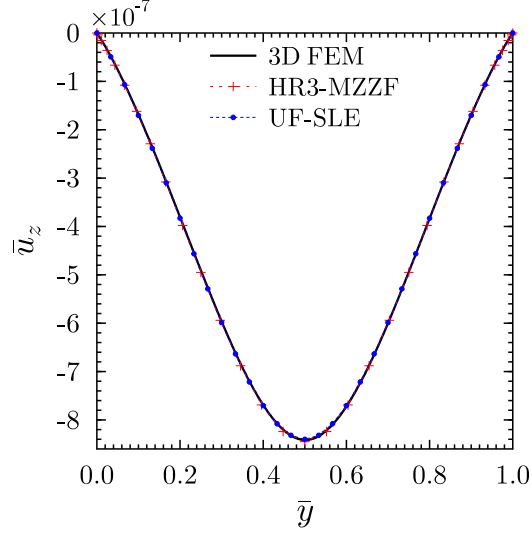


(c) Transverse shear stress, $\bar{\tau}_{yz}$ at $y = L/4$

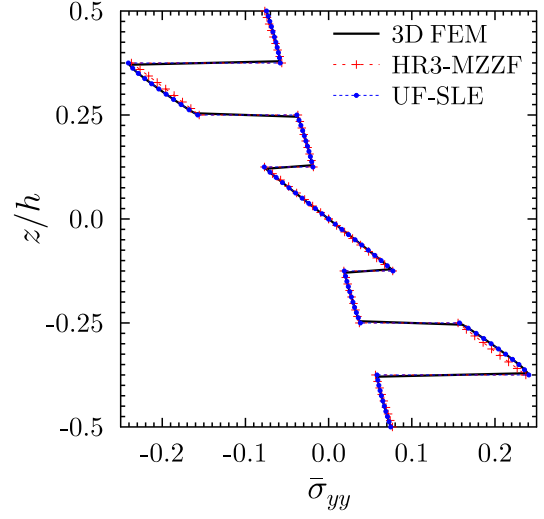


(d) Transverse normal stress, $\bar{\sigma}_{zz}$ at $y = L/2$

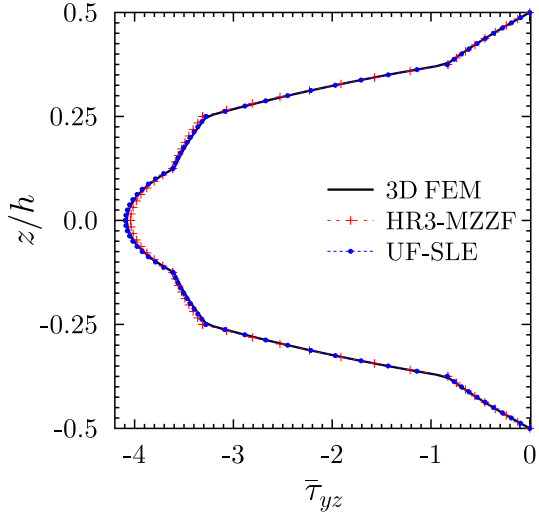
Figure 4: Normalised bending deflection and through-thickness distribution of the normalized axial and transverse stresses for VAT laminate A.



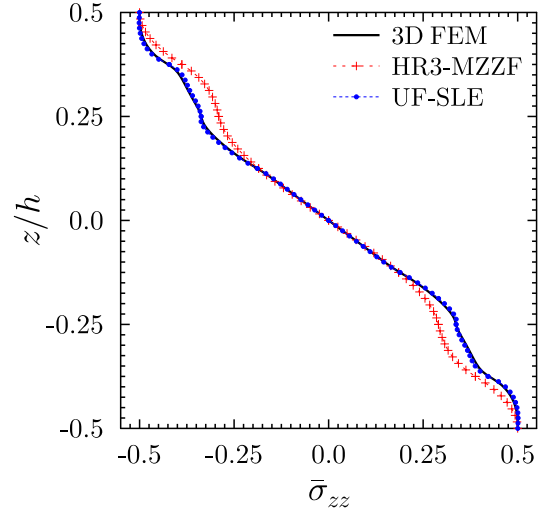
(a) Normalised bending deflection, \bar{u}_z



(b) Axial normal stress, $\bar{\sigma}_{yy}$ at $y = L/2$

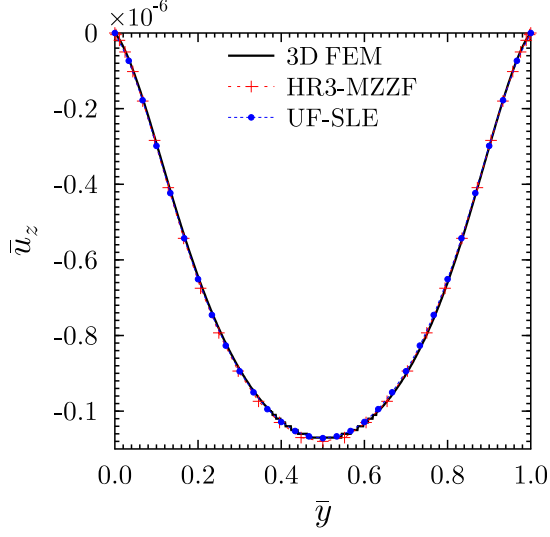


(c) Transverse shear stress, $\bar{\tau}_{yz}$ at $y = L/4$

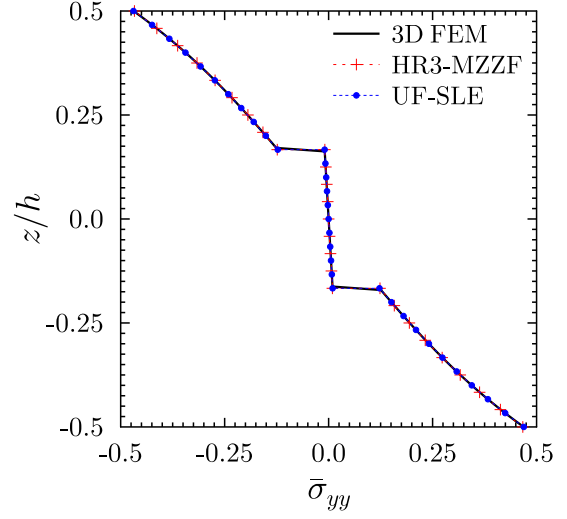


(d) Transverse normal stress, $\bar{\sigma}_{zz}$ at $y = L/2$

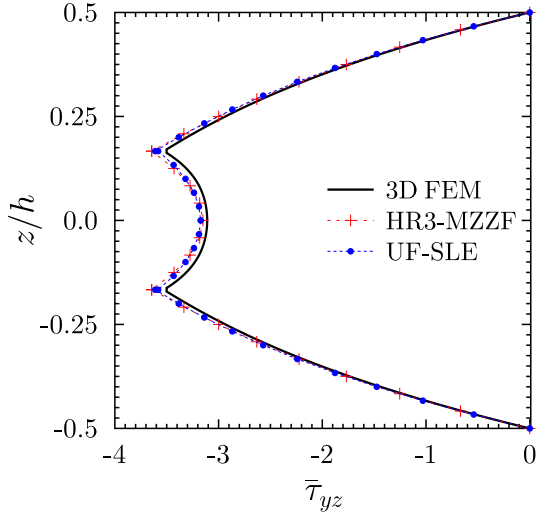
Figure 5: Normalised bending deflection and through-the-thickness distribution of the normalized axial and transverse stresses for VAT laminate B.



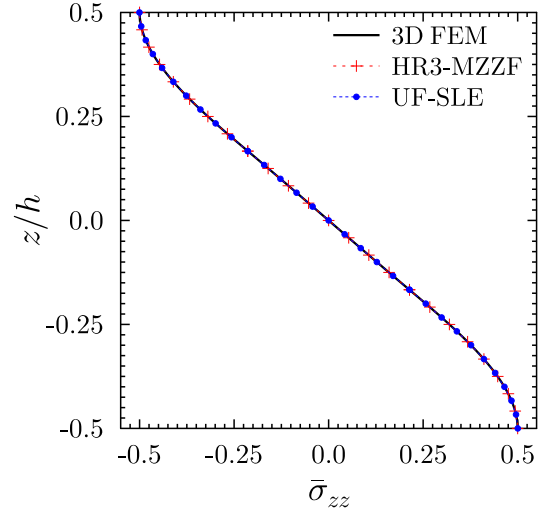
(a) Normalised bending deflection, \bar{u}_z



(b) Axial normal stress, $\bar{\sigma}_{yy}$ at $y = L/2$

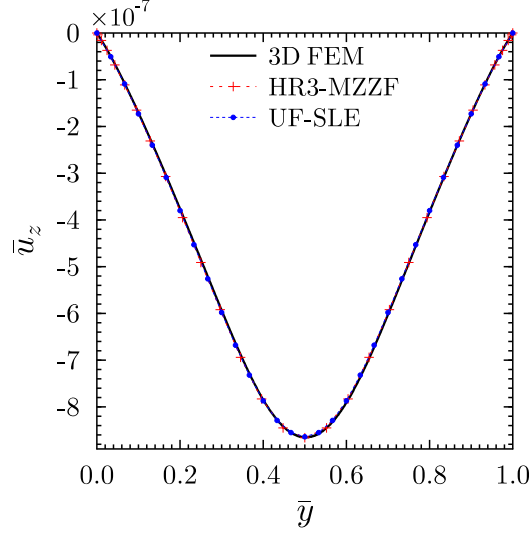


(c) Transverse shear stress, $\bar{\tau}_{yz}$ at $y = L/4$

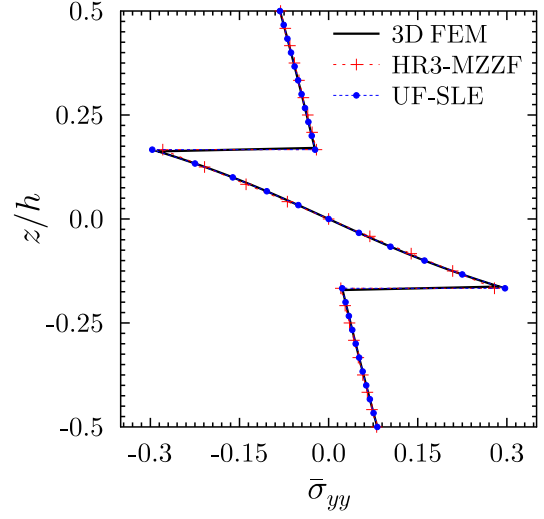


(d) Transverse normal stress, $\bar{\sigma}_{zz}$ at $y = L/2$

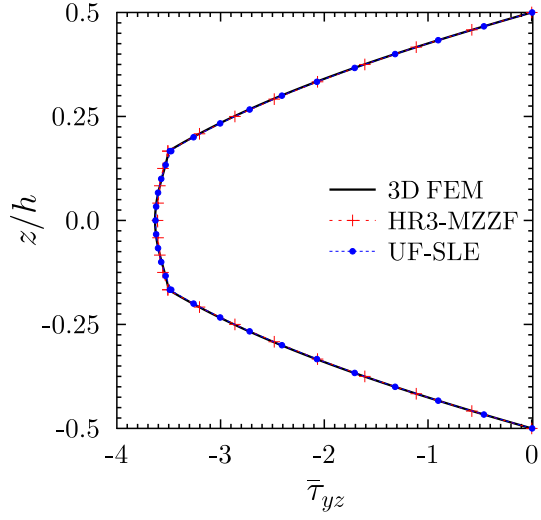
Figure 6: Normalised bending deflection and through-thickness distribution of the normalized axial and transverse stresses for VAT laminate C.



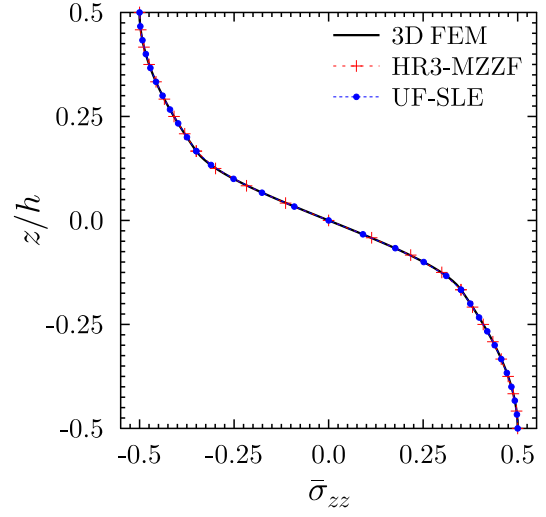
(a) Normalised bending deflection, \bar{u}_z



(b) Axial normal stress, $\bar{\sigma}_{yy}$ at $y = L/2$

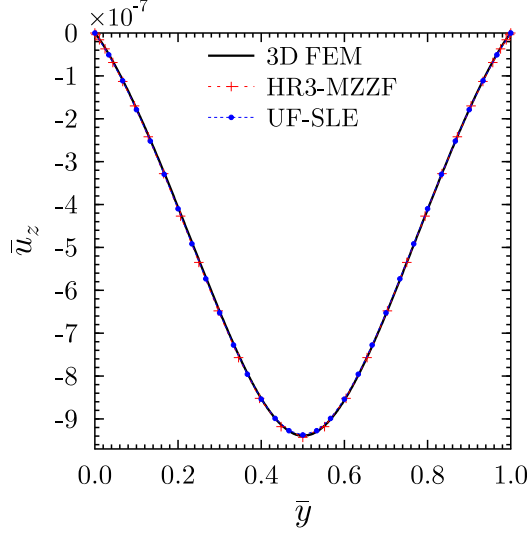


(c) Transverse shear stress, $\bar{\tau}_{yz}$ at $y = L/4$

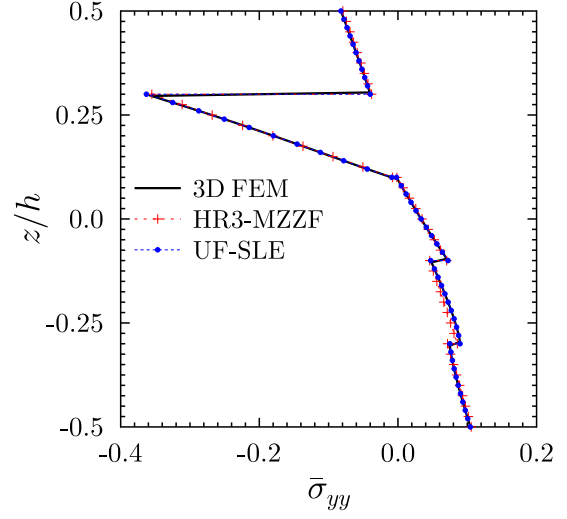


(d) Transverse normal stress, $\bar{\sigma}_{zz}$ at $y = L/2$

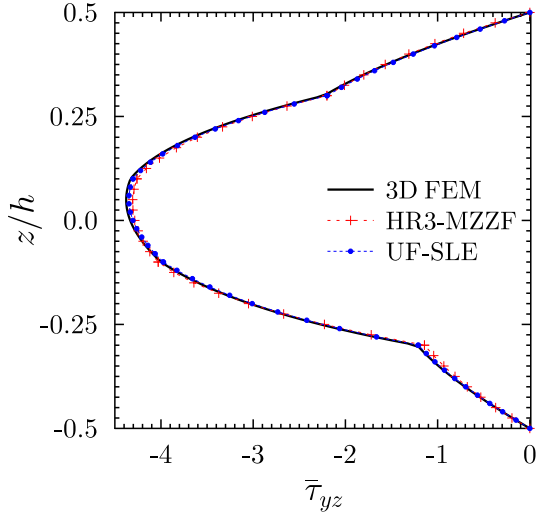
Figure 7: Normalised bending deflection and through-thickness distribution of the normalized axial and transverse stresses for VAT laminate D.



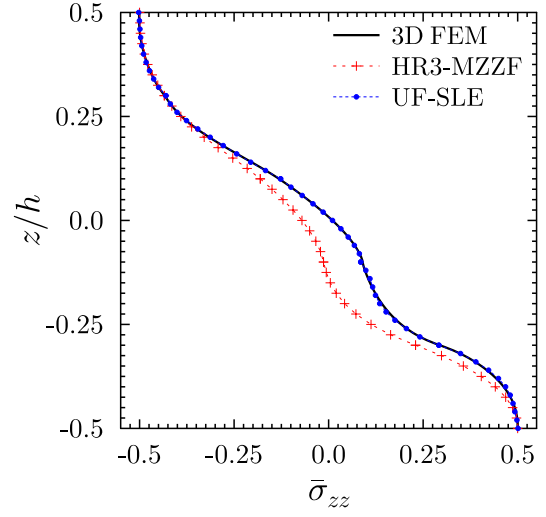
(a) Normalised bending deflection, \bar{u}_z



(b) Axial normal stress, $\bar{\sigma}_{yy}$ at $y = L/2$

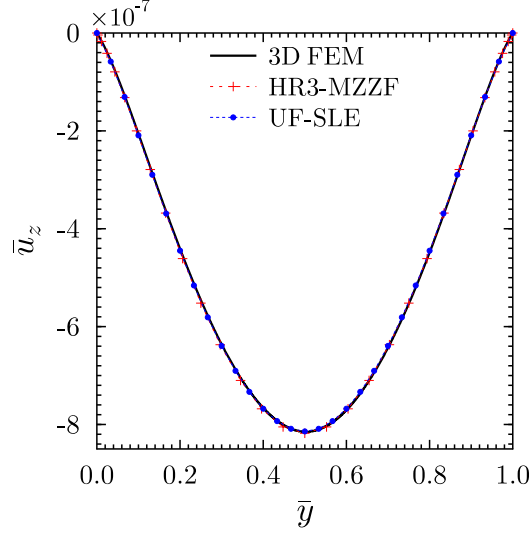


(c) Transverse shear stress, $\bar{\tau}_{yz}$ at $y = L/4$

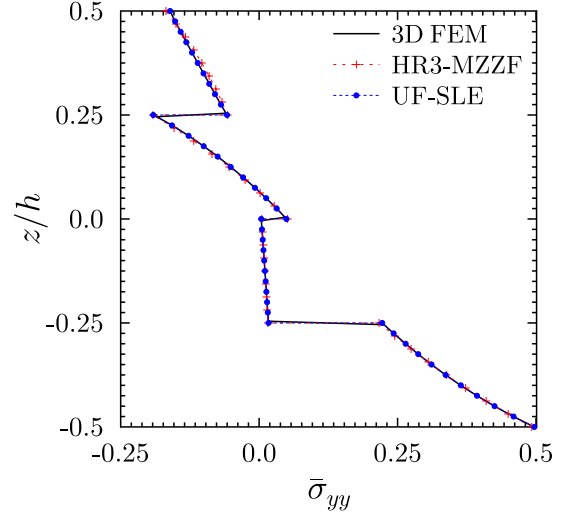


(d) Transverse normal stress, $\bar{\sigma}_{zz}$ at $y = L/2$

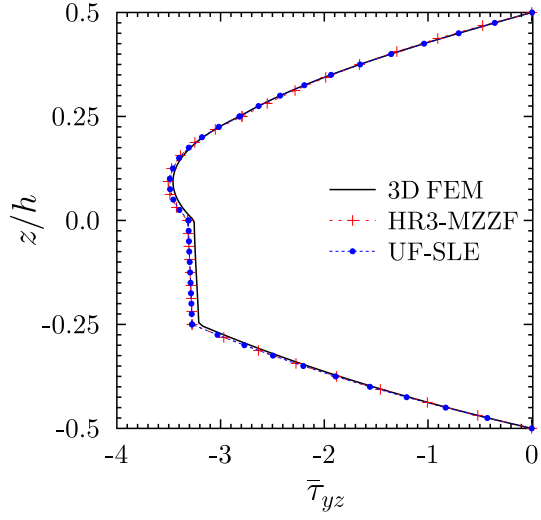
Figure 8: Normalised bending deflection and through-thickness distribution of the normalized axial and transverse stresses for VAT laminate E.



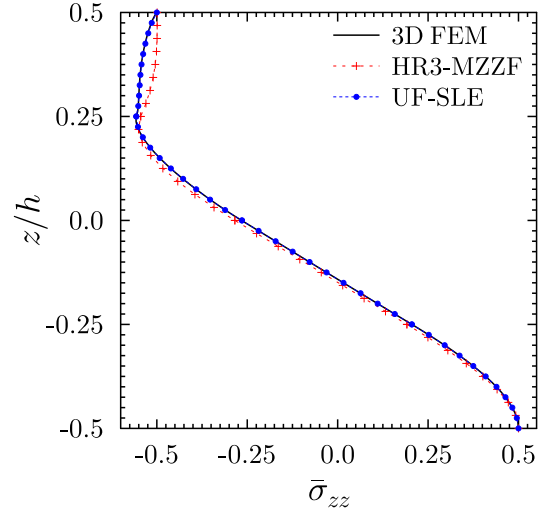
(a) Normalised bending deflection, \bar{u}_z



(b) Axial normal stress, $\bar{\sigma}_{yy}$ at $y = L/2$

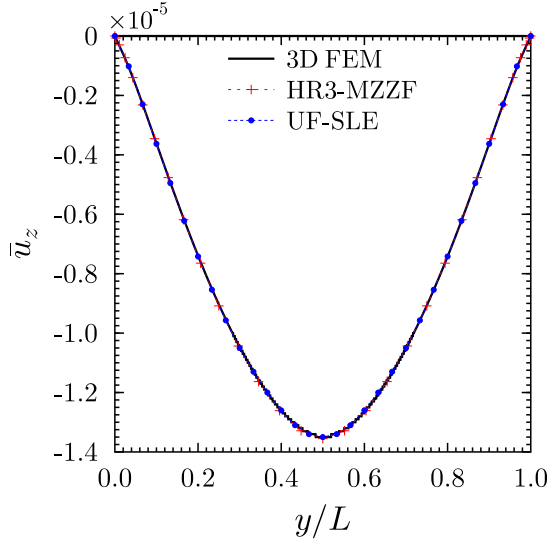


(c) Transverse shear stress, $\bar{\tau}_{yz}$ at $y = L/4$

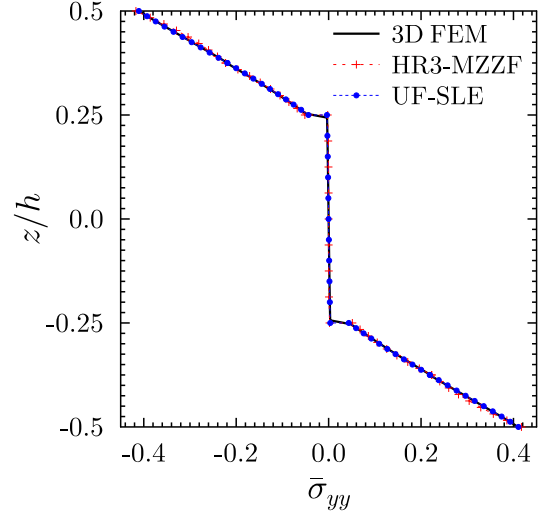


(d) Transverse normal stress, $\bar{\sigma}_{zz}$ at $y = L/2$

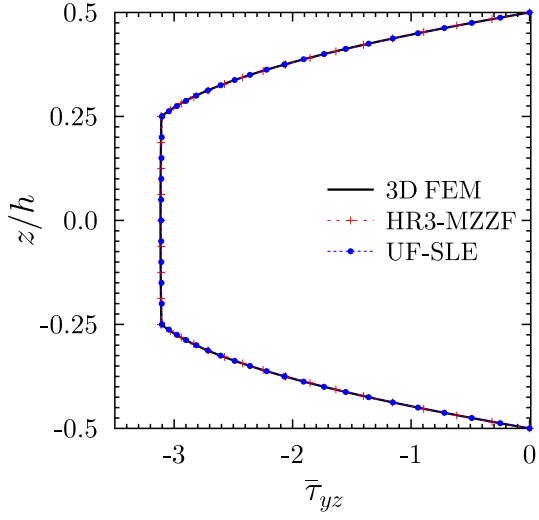
Figure 9: Normalised bending deflection and through-the-thickness distribution of the normalized axial and transverse stresses for VAT laminate F.



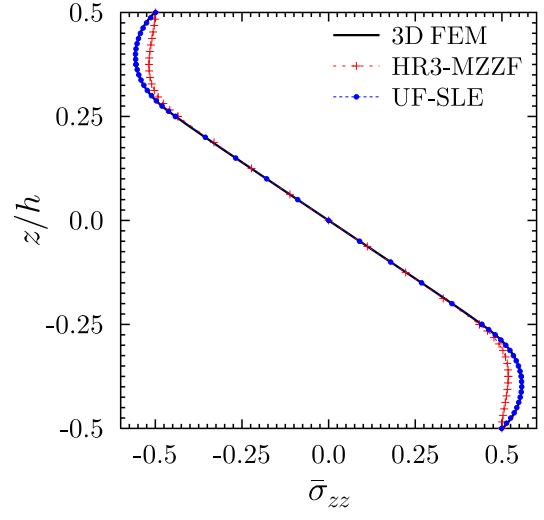
(a) Normalised bending deflection, \bar{u}_z



(b) Axial normal stress, $\bar{\sigma}_{yy}$ at $y = L/2$

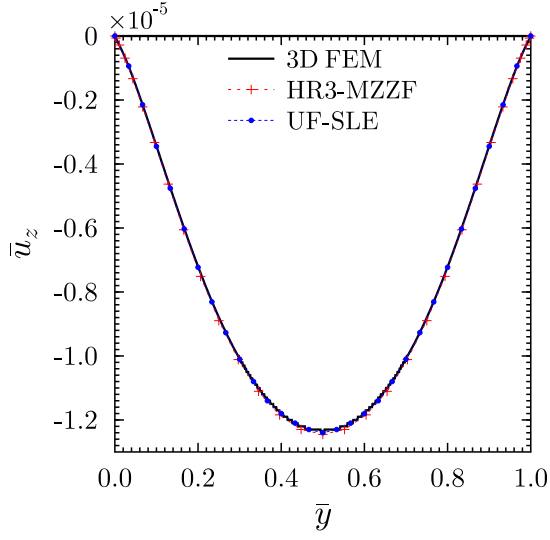


(c) Transverse shear stress, $\bar{\tau}_{yz}$ at $y = L/4$

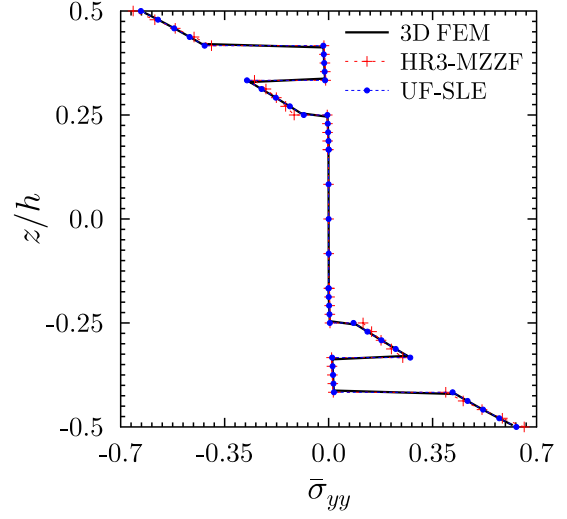


(d) Transverse normal stress, $\bar{\sigma}_{zz}$ at $y = L/2$

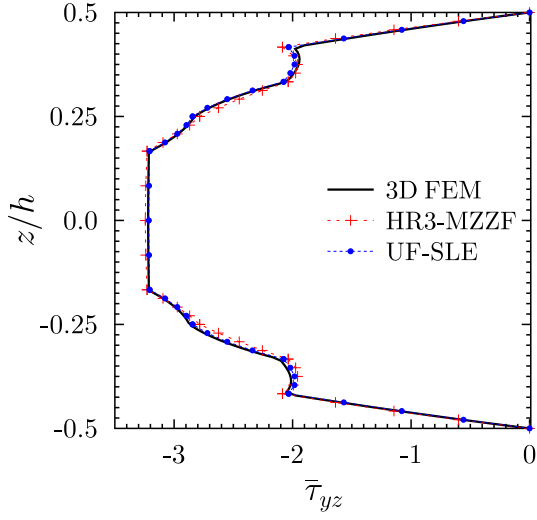
Figure 10: Normalised bending deflection and through-thickness distribution of the normalized axial and transverse stresses for VAT laminate G.



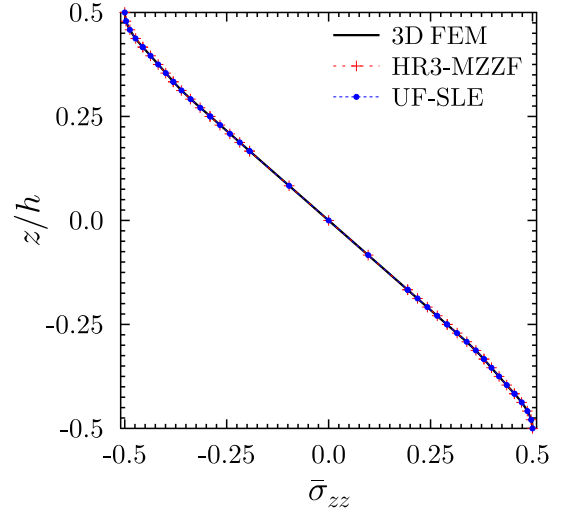
(a) Normalised bending deflection, \bar{u}_z



(b) Axial normal stress, $\bar{\sigma}_{yy}$ at $y = L/2$

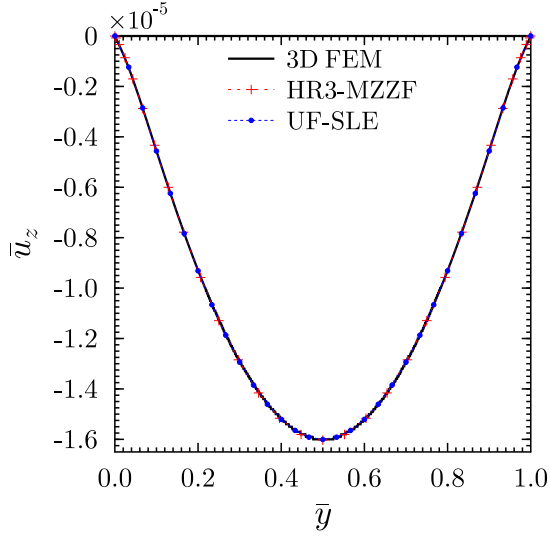


(c) Transverse shear stress, $\bar{\tau}_{yz}$ at $y = L/4$

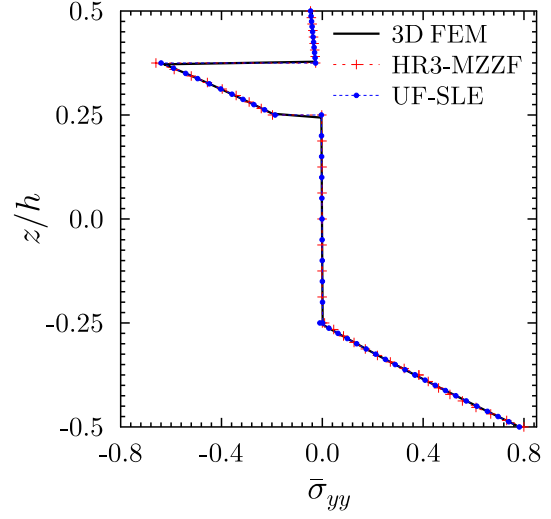


(d) Transverse normal stress, $\bar{\sigma}_{zz}$ at $y = L/2$

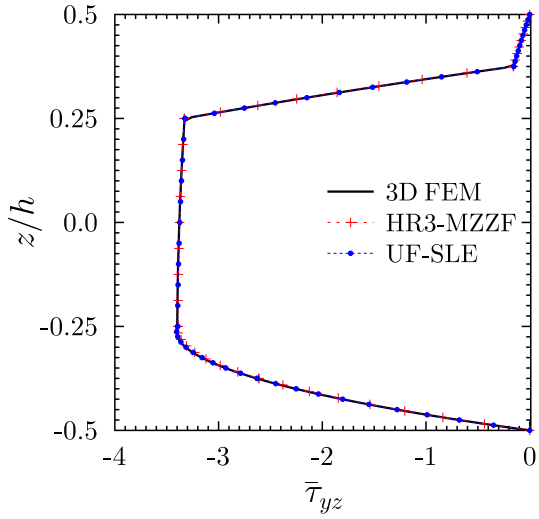
Figure 11: Normalised bending deflection and through-thickness distribution of the normalized axial and transverse stresses for VAT laminate H.



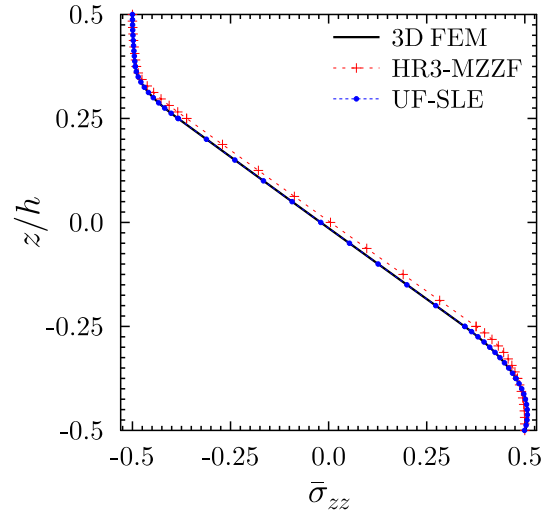
(a) Normalised bending deflection, \bar{u}_z



(b) Axial normal stress, $\bar{\sigma}_{yy}$ at $y = L/2$

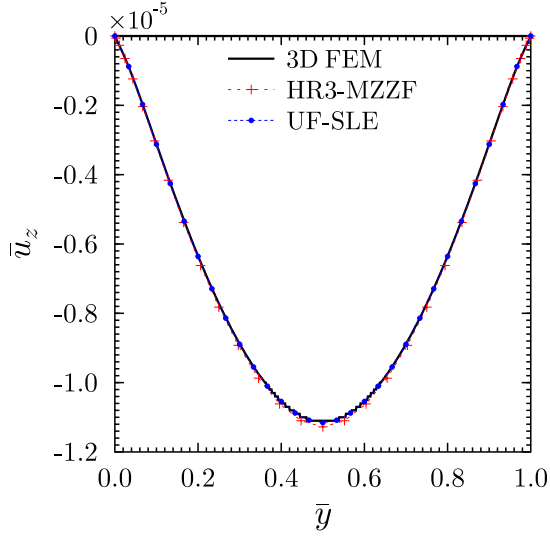


(c) Transverse shear stress, $\bar{\tau}_{yz}$ at $y = L/4$

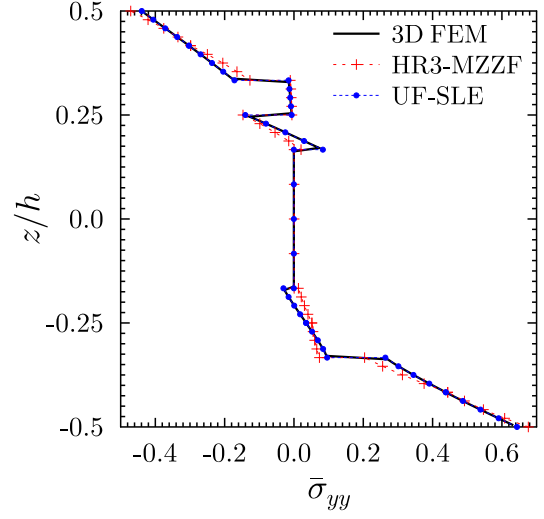


(d) Transverse normal stress, $\bar{\sigma}_{zz}$ at $y = L/2$

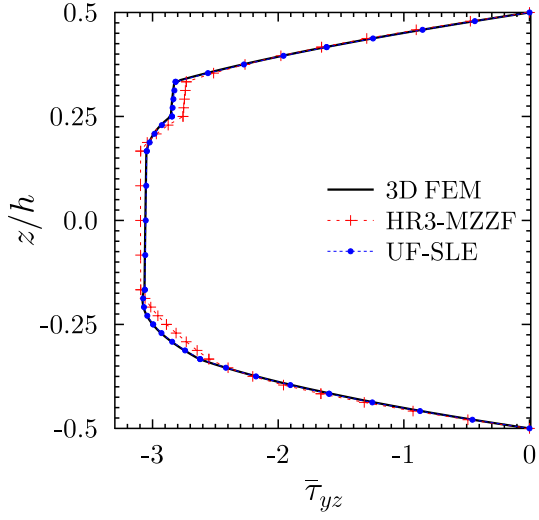
Figure 12: Normalised bending deflection and through-thickness distribution of the normalized axial and transverse stresses for VAT laminate I.



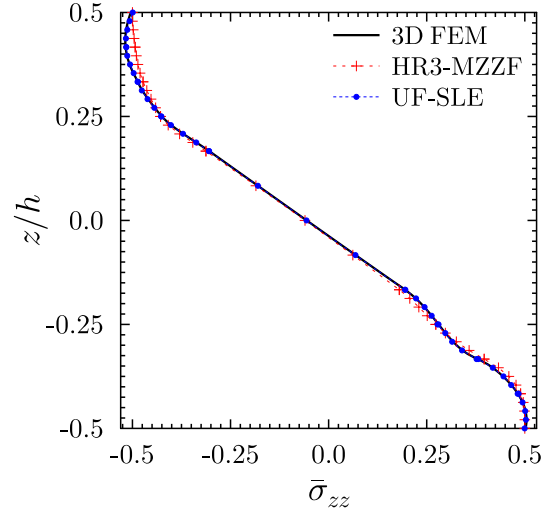
(a) Normalised bending deflection, \bar{u}_z



(b) Axial normal stress, $\bar{\sigma}_{yy}$ at $y = L/2$



(c) Transverse shear stress, $\bar{\tau}_{yz}$ at $y = L/4$



(d) Transverse normal stress, $\bar{\sigma}_{zz}$ at $y = L/2$

Figure 13: Normalised bending deflection and through-thickness distribution of the normalized axial and transverse stresses for VAT laminate J.

equations for all VAT beams A-J in case of the 3D FE and the HR model. In addition to the residual, the total strain energy was also used to assess the accuracy of the two models. These quantitative findings clearly showed that the HR model obeys the stress equilibrium equations more accurately, and at the same time corresponds to a lower strain energy configuration than 3D FE. Hence, it was inferred that the HR3-MZZF solution provides a more accurate representation of the 3D stress field within the structures analysed than the purely displacement-based 3D FE formulation. However, let us now consider the transverse stress plots for VAT beams F, G and J (Figures 9, 10 and 13), which show the greatest discrepancy between the two weak, displacement-based formulations (3D FE and the UF-SLE) and the HR model. Groh & Weaver [36] originally argued that the 3D FE model does not obey the traction equilibrium condition on the top and bottom surfaces (top for F and J, top and bottom for G). Their argument was based on analysing Cauchy's transverse equilibrium equation in the absence of body forces as given by

$$\frac{\partial \tau_{xz}}{\partial x} + \frac{\partial \tau_{yz}}{\partial y} + \frac{\partial \sigma_{zz}}{\partial z} = 0, \quad (12)$$

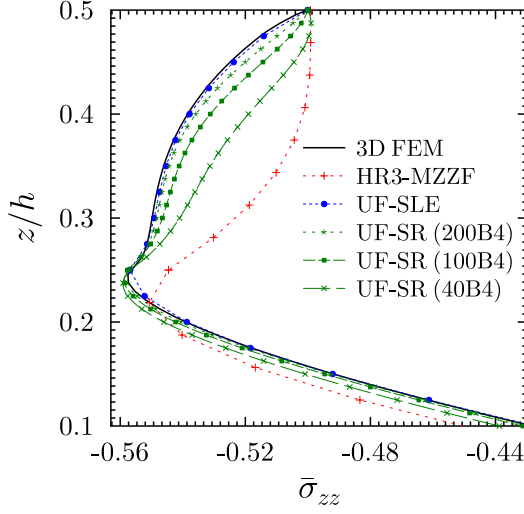
and went as follows. The test case considered here assumes a plane strain condition in the lateral x -direction, hence $\tau_{xz} = 0$. Also, due to the absence of shear tractions on the top and bottom surfaces, $\tau_{yz}(z = \pm h/2) = 0$. It follows that the axial derivative of the transverse shear stress vanishes on the top and bottom surfaces, $\partial \tau_{yz} / \partial y (z = \pm h/2) = 0$. Groh & Weaver therefore argued that the z -wise derivative of the transverse normal stress $\partial \sigma_{zz} / \partial z$ must be zero at the top and bottom surfaces. The plots of $\bar{\sigma}_{zz}$ in Figures 9, 10 and 13 show that this condition does not hold true for the 3D FE and the UF-SLE model, whereas the HR3-MZZF model satisfies this boundary condition for all cases. However, for a 3D body, Eq. (12) describes the equilibrium within the interior of the continuum, whereas the top and bottom surfaces are on the boundary. Hence, Eq. (12) is in fact not applicable at these points and only the traction boundary conditions need to be satisfied. Both 3D FE and UF-SLE models satisfy the transverse traction conditions. Even though the z -wise derivative of the transverse normal stress $\partial \sigma_{zz} / \partial z$ is often zero for isotropic structures and straight-fibre laminates, the traction boundary conditions do not require this to be so, and indeed for some VAT laminates (F, G and J) the condition does not hold.

To elucidate this point further we compute the transverse normal stress using the UF-SLE model, not from the constitutive relation, but from the transverse stress equilibrium equation, hence mimicking the HR approximation. This approach is commonly termed as Stress Recovery (SR), which ensures that the 3D stress equilibrium equations are satisfied. The stress recovery technique applied in the Unified formulation framework is detailed in [39]. The transverse normal stress recovered is shown as the ‘‘UF-SR (40B4)’’ curve in Figure 14, a close-up on surface stresses for VAT beams F and G. It is observed that the through-thickness gradient of $\bar{\sigma}_{zz}$ approaches zero at the top surface. However, with an increase in the number of beam elements along the length from 40 to 200 it is observed, in contrast, that the curve progressively approaches the transverse normal stress distribution obtained from 3D FE and UF-SLE models (using the constitutive relation). From these results, a couple of important conclusions can be drawn. Firstly, the initial solution obtained from the constitutive relations has already converged and there is no further need to employ the SR step. Secondly, the shift in the curve of $\bar{\sigma}_{zz}$ (obtained by SR) with increasing beam elements indicates that the spanwise distribution of the transverse shear stress is indeed varying such as to satisfy equilibrium (Eq. 12).

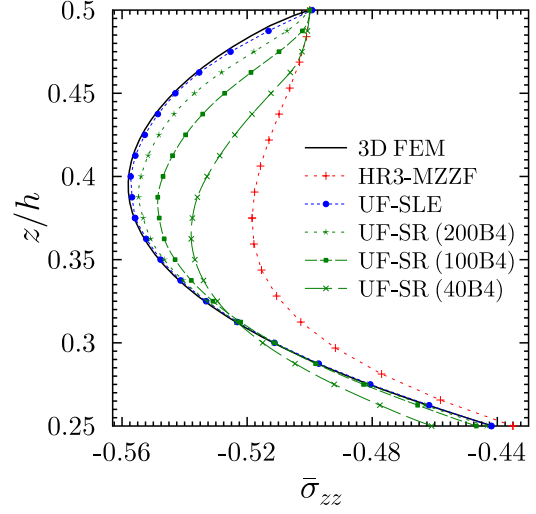
Shifting our attention on the transverse shear stress, Figure 15a shows the variation of $\bar{\tau}_{yz}$ along the beam, just below the top surface ($z/h = 0.499$). The distribution is shown to be continuous but non-differentiable at the mid-span of the beam. A similar behaviour is observed by plotting the variation of $\bar{\sigma}_{yy}$ in Figure 15b, implying that $\frac{\partial \sigma_{yy}}{\partial y}$ and $\frac{\partial \tau_{yz}}{\partial y}$ are not defined at $y = L/2$. For the same reason one can deduce that the residuals

$$\frac{\partial \tau_{xy}}{\partial x} + \frac{\partial \sigma_{yy}}{\partial y} + \frac{\partial \tau_{yz}}{\partial z} = R_y, \quad \frac{\partial \tau_{xz}}{\partial x} + \frac{\partial \tau_{yz}}{\partial y} + \frac{\partial \sigma_{zz}}{\partial z} = R_z, \quad (13)$$

are also not defined at $y = L/2$. This hypothesis is examined quantitatively and confirmed by plotting residuals R_y and R_z at various locations along the beam length, just below the top surface ($z/h = 0.499$) in Figure 16. Therefore, in such cases the stress distribution is incorrect if recovered from Cauchy's equilibrium



(a) VAT beam F: Transverse normal stress, $\bar{\sigma}_{zz}$



(b) VAT beam G: Transverse normal stress, $\bar{\sigma}_{zz}$

Figure 14: A close-up plot focusing on the distribution of the normalized transverse normal stress near the top surface at $y = L/2$, for VAT laminates F and G.

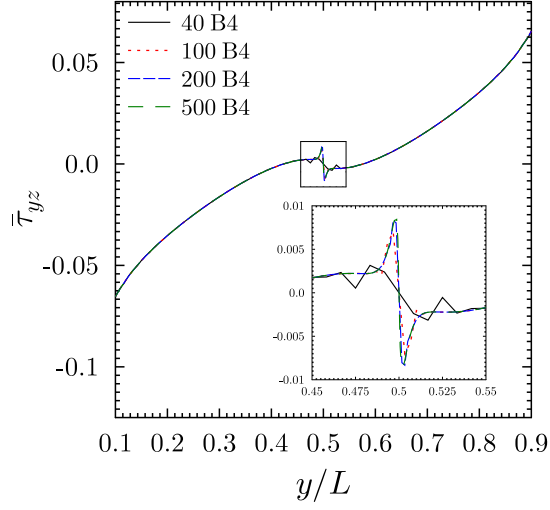
equations. The HR formulation uses a similar approach as the SR technique as Cauchy's equilibrium equations are used to inform the stress assumptions, and incorrectly enforces field equilibrium rather than boundary (traction) equilibrium on the top and bottom surface. Hence, the normal stress distribution obtained from the HR3-MZZF model at the beam's mid-span is inaccurate for VAT laminates F, G and J, and the through-thickness gradient of $\bar{\sigma}_{zz}$ is not zero towards the surfaces, as correctly obtained from 3D FE and UF-SLE models. At locations other than the mid-span, since $\frac{\partial \tau_{yz}}{\partial y}$ is defined, a boundary layer, defined as the region below the top surface up to the point where $\frac{\partial \sigma_{zz}}{\partial z}$ goes to zero, does exist. The boundary layer thickness, t_{BL} , calculated from the top surface is shown in Figure 17.

The reason for $\bar{\tau}_{yz}$ and $\bar{\sigma}_{yy}$ to be continuous but non-differentiable at the mid-span is the linear fibre angle variation definition by Gürdal and Olmedo [1]. This is illustrated by Figures 18 and 19a. The former shows the representation of spatially steered fibres in the plane of a composite lamina, while Figure 19a shows the spanwise variation of fibre angle as calculated from Eq. 10 for different combinations of $T_0|T_1$. One of the combinations considered is for the top layer of VAT beam G, where the fibre angle starts at -45° , is steered linearly to 45° at the mid-span, and then ends at -45° . In other cases, T_0 is varied from 0° to 90° , while T_1 is kept fixed at -45° , so as to understand the reason for the typical behaviour observed at the beam's mid-span. Figures 19d and 19e show the spanwise variation of the transformed in-plane normal stiffness \bar{C}_{22} and transverse shear stiffness \bar{C}_{44} . Mathematically, the transformed elastic coefficients \bar{C}_{22} and \bar{C}_{44} for an orthotropic material, can be obtained from the elastic coefficients in the material coordinates C_{ij} by means of Eq. 14 [48],

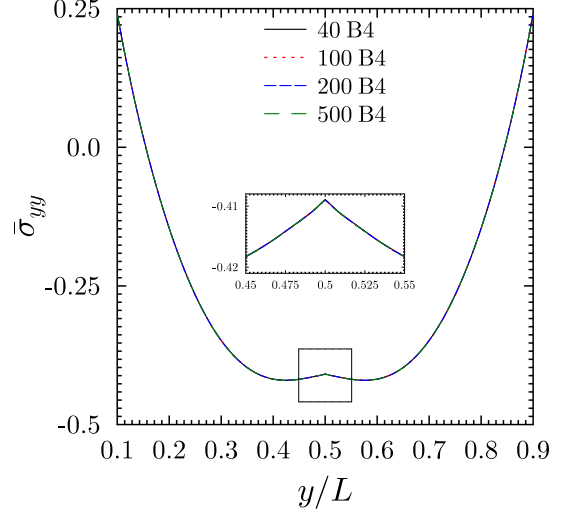
$$\begin{aligned}\bar{C}_{22} &= C_{22} \cos^4 \theta_y + 2(C_{11} + 2C_{66}) \cos^2 \theta_y \sin^2 \theta_y + C_{11} \sin^4 \theta_y, \\ \bar{C}_{44} &= C_{44} \cos^2 \theta_y + C_{55} \sin^2 \theta_y,\end{aligned}\tag{14}$$

where $\theta_y = \theta(y)$ is the fibre angle orientation. Substituting the expression of \bar{C}_{44} from Eq. 14 in Eq. 29 of Appendix B, the expression of transverse shear stress and its derivative with respect to the y -coordinate can be written as

$$\begin{aligned}\tau_{yz} &= \bar{C}_{44} \gamma_{yz}, \\ \frac{\partial \tau_{yz}}{\partial y} &= \gamma_{yz} \frac{\partial \bar{C}_{44}}{\partial y} + \bar{C}_{44} \frac{\partial \gamma_{yz}}{\partial y}.\end{aligned}\tag{15}$$

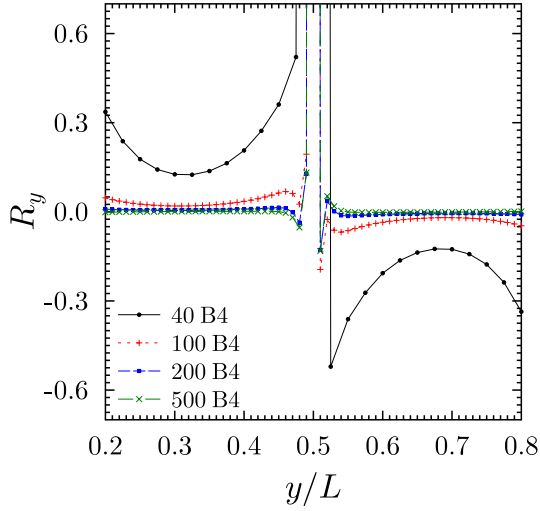


(a) Transverse shear stress, $\bar{\tau}_{yz}$

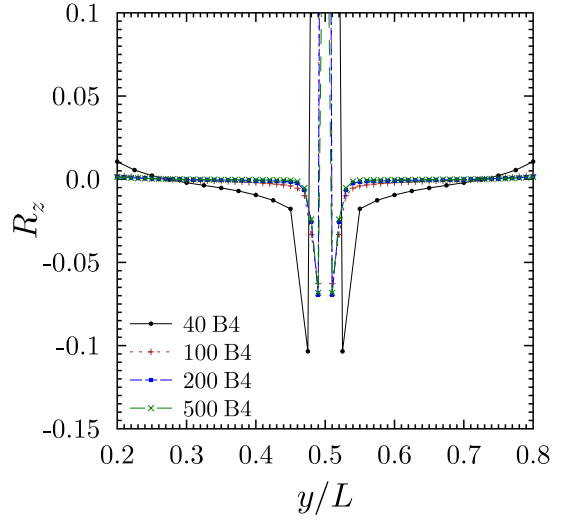


(b) Axial normal stress, $\bar{\sigma}_{yy}$

Figure 15: Variation of transverse shear and axial normal stresses along the beam length $y/L \in [0.1, 0.9]$ at $z/h = 0.499$ (just below the top surface) for VAT laminate G as calculated from the UF-SLE model.



(a) Residual, R_y



(b) Residual, R_z

Figure 16: Spanwise distribution of residuals of Cauchy's y - and z -direction equilibrium equations just below the top surface at $z/h = 0.499$ for VAT laminate G as calculated from the UF-SLE model.

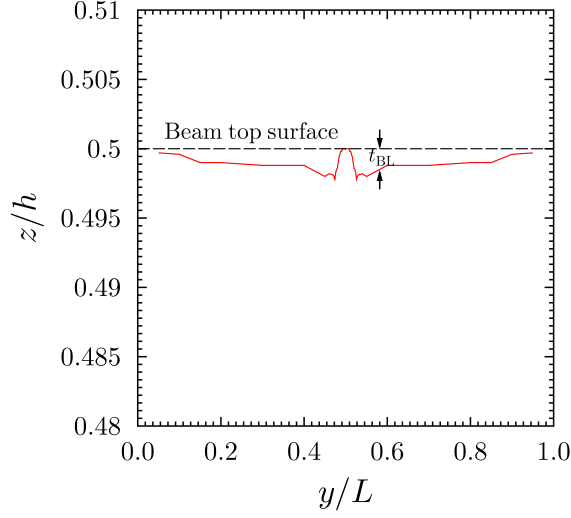


Figure 17: The boundary layer below the top surface along the beam length for VAT laminate G as calculated from the UF-SLE model.

In case of straight fibre laminates, $\frac{\partial \bar{C}_{44}}{\partial y} = 0$. But for a VAT laminate $\frac{\partial \bar{C}_{44}}{\partial y}$ is given by

$$\begin{aligned} \frac{\partial \bar{C}_{44}}{\partial y} &= -C_{44} \sin(2\theta_y) \frac{\partial \theta_y}{\partial y} + C_{55} \sin(2\theta_y) \frac{\partial \theta_y}{\partial y}, \\ &= (C_{55} - C_{44}) \sin(2\theta_y) \frac{\partial \theta_y}{\partial y}. \end{aligned} \quad (16)$$

Clearly, Eq. 16 and Figure 19a, show that $\frac{\partial \theta_y}{\partial y}$ does not exist at $y = L/2$ because this is the apex of the absolute function that describes θ_y in Eq. 10. Indeed, Figures 19b and 19c show the nature of the fibre angle slope and curvature at the midspan as a Heaviside function and Dirac function, respectively. If Cauchy's equilibrium equations are therefore used across this fibre angle singularity at the midspan, then the derivatives are incorrectly computed numerically. Hence, under such circumstances, both, the SR technique and the HR model, lead to incorrect results. In fact, because there is a constitutive singularity at the midspan, the continuity condition of a continuum is broken such that the midspan needs to be treated as a boundary and not as an interior point. This condition is inherently satisfied in 3D FE and UF-SLE models if an elemental boundary node is placed at the midspan and the transverse stress results are computed from the underlying constitutive equations.

This study highlights crucial intricacies in modelling VAT laminates. Even though the structure may seem like a global continuum, singularities in the angle description can break the fundamental assumptions underlying a mechanical continuum, such that internal boundaries need to be placed within the structure to correctly model its mechanical behaviour. Such behaviour leads to highly localised raised levels of transverse shear stress (see Figure 15) with ensuing implications for failure prediction and design. Indeed, such considerations are necessary whenever a linear variation of fibre orientation is used (Eq. 10). Appropriate mechanical response is accomplished using a weak-form finite element approach as long as exterior elemental nodes are placed at singularity locations. Furthermore, this discussion addresses the issues regarding discrepancies between HR3-MZZF and UF-SLE models in computing the transverse normal stress $\bar{\sigma}_{zz}$ for VAT beams A, B, E, F, G, I and J. The discrepancies occur at specific positions through the thickness, where the fibre angle at the mid-span T_0 differs from 0° and 90° , as shown in Figures 4d, 5d, 8d, 9d, 10d, 12d and 13d. For the VAT beams C, D and H, all layers have T_0 values with either 0° or 90° , so that the transverse normal stress correlates well for all models as shown in Figures 6d, 7d and 11d.

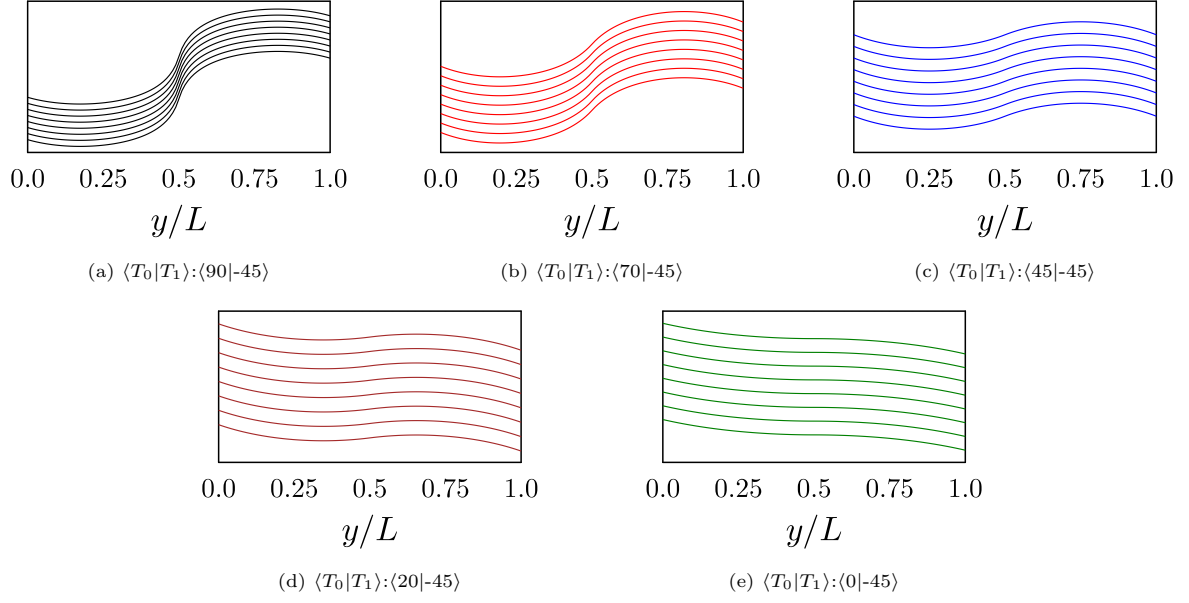


Figure 18: Representation of spatially steered fibres in the plane of a composite lamina for various combinations of T_0 and T_1 .

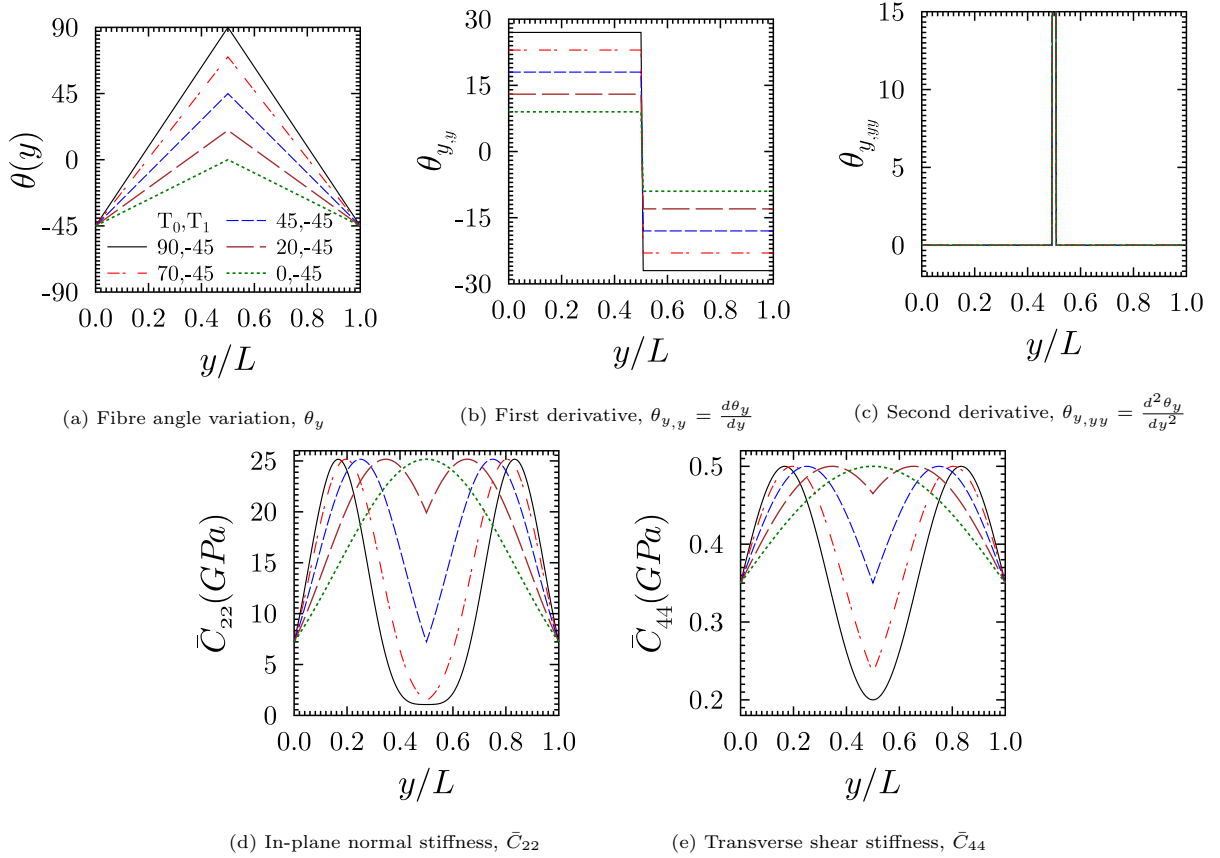


Figure 19: Spanwise distribution of (a) fibre angle, (b) first derivative of fibre angle, (c) second derivative of fibre angle (d) in-plane normal stiffness term and (e) transverse shear stiffness term for various combinations of T_0 and T_1 .

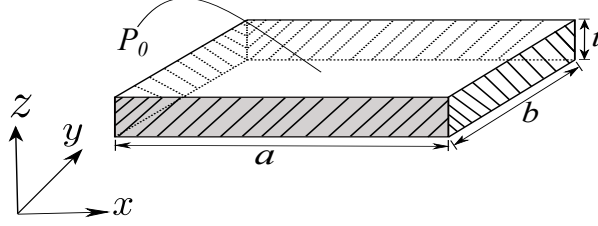


Figure 20: Representation of a laminated square plate-like structure ($a/t = b/t = 10$), clamped along all four faces and subjected to a uniformly distributed load at the top surface.

3.2. Tow-Steered Composite Plate-like Structure

This section aims to assess the capability of the UF-SLE model in computing the 3D stress fields in tow-steered plates and compares these against 3D FE and HR3-MZZF models. Consider a square plate-like 3D structure, as shown in Figure 20, with side length-to-thickness ratio $a/t = b/t = 10$. The plate comprises N_l orthotropic, tow-steered laminae of arbitrary thickness t^k with the fibre orientation angle $\theta^k(y)$ varying linearly along the y -direction as given by Eq. 10. The plate is clamped along all four faces and is subjected to a uniformly distributed pressure load, P_0 , on the top surface. The laminates investigated here are restricted to symmetric stacking sequences for both composites and sandwich plates, designated as VAT K, L and M. The material properties and stacking sequences are shown in Tables 1 and 2.

In the UF-SLE model, the plate structure is discretised with 20 B4 elements along the length (y -direction), whereas the cross-section is divided into $3 \times N_l$ sub-domains (three elements along the x -direction and one element per layer). Within each sub-domain (Serendipity Lagrange element), a seventh-order expansion is employed. The number of elements and the order of expansion are prescribed by performing a convergence analysis. The model is verified against 3D FE analysis performed in ABAQUS [36], where the structure is meshed with 1,776,080 linear C3D8R reduced integration brick elements. All stress results are presented as normalised metrics, which are defined as follows:

$$\begin{aligned} \bar{\sigma}_{xx} &= \frac{t^2}{P_0 a^2} \cdot \sigma_{xx}(x, y, z), & \bar{\sigma}_{yy} &= \frac{t^2}{P_0 b^2} \cdot \sigma_{yy}(x, y, z), & \bar{\tau}_{xy} &= \frac{t^2}{P_0 ab} \cdot \tau_{xy}(x, y, z), \\ \bar{\tau}_{xz} &= \frac{1}{P_0} \cdot \tau_{xz}(x, y, z), & \bar{\tau}_{yz} &= \frac{1}{P_0} \cdot \tau_{yz}(x, y, z), & \bar{\sigma}_{zz} &= \frac{1}{P_0} \cdot \sigma_{zz}(x, y, z). \end{aligned} \quad (17)$$

Through-thickness variations of all six stress fields for VAT plates K, L and M are plotted in Figures 21 to 23. The planar (x, y) locations of each plot are indicated in the figure captions.

The transverse pressure applied on the top surface locally affects the in-plane stress field due to Poisson's coupling. This local effect is pronounced for VAT K and is clearly shown in the in-plane $\bar{\sigma}_{xx}$ stress plot (Figure 21), where the compressive stress on the top surface is greater than the tensile stress on the bottom surface. The UF-SLE model, being hierarchical in nature, allows higher-order terms to be readily added to the displacement field approximation, and is therefore capable of capturing these localised effects more readily compared to the HR3-MZZF model, which is based on a third-order equivalent single-layer theory. Furthermore, for sandwich plate VAT M, the accuracy obtained with the present modelling approach is superior in contrast to the HR3-MZZF model, particularly for in-plane stress fields $\bar{\sigma}_{xx}$, $\bar{\sigma}_{yy}$ and $\bar{\tau}_{xy}$, as shown in Figure 23. For all VAT composite and sandwich plates analysed herein, the UF-SLE model results correlate better with the 3D FE solutions than to those obtained by the HR3-MZZF model.

3.3. Computational Efficiency Gain over 3D FE Model

To analyse tow-steered composite structures, a 3D finite element model requires a refined in-plane mesh to guarantee sufficiently smooth fibre variations after discretisation. Additionally, the limitation on the aspect ratio of a 3D brick element further necessitates a refined mesh in the thickness direction, which thereby

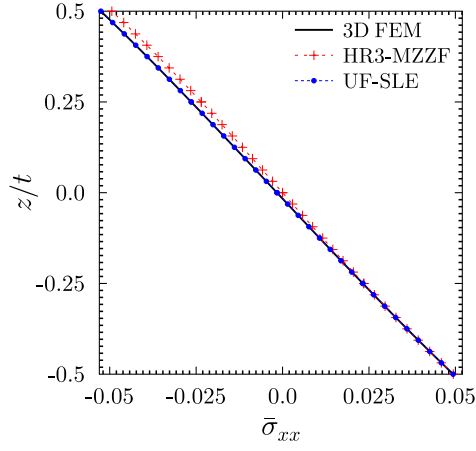
increases the overall mesh density. In contrast, the UF-SLE model describes the fibre variation smoothly, as the angle is defined at Gauss points and is interpolated using the traditional cubic 1D Lagrange shape functions within the element. Moreover, as discussed in Section 2.2, decoupling the shape functions along the longitudinal axis from the transverse plane removes the limitation of maintaining square element aspect ratios. Hence, the UF-SLE approach has certain advantages in analysing VAT laminated structures in a computationally efficient manner. The authors' previous work highlighted the computational efficiency of the UF-SLE model compared to 3D finite elements for laminated composite and sandwich structures [39]. For comparison purposes, computational time and algebraic system complexity were measured, which quantify the amount of time and storage required by an algorithm. In the present study, we compare the degrees of freedom (or the number of unknown variables) required to solve the system, which gives an estimate of the relative time and space complexity and thus, predicts overall computational efficiency.

The deflection and stress response obtained for VAT beams A-J, presented in Section 3.1, are computed by discretising the structure with 95,880 linear C3D8R elements in ABAQUS, which results in 580,800 DOFs. On the other hand, a fourth-order SLE model with one cross-section element per layer is used within the Unified Formulation framework with 40 B4 elements along its length to obtain the structural response as shown in Figures 4 to 13. This setting results in 14,883 DOFs (lowest) and 41,019 DOFs (highest) for VAT D (3 layers) and VAT H, J (9 layers), respectively. Furthermore, accurately computing the localised 3D stress fields in VAT plates K-M demands high-fidelity models. Therefore, in the case of 3D FE analysis, 1,776,080 linear C3D8R elements are used, resulting in 5,467,500 DOFs, and a seventh-order SLE model is employed in the UF framework with 20 B4 elements, leading to 129,198 DOFs for VAT M (9 layers). These numbers clearly demonstrate the computational benefit attained by using the UF-SLE model over the 3D FE model. On the other hand, the HR model is slightly less accurate than the SLE approach but also requires an order of magnitude fewer DOFs.

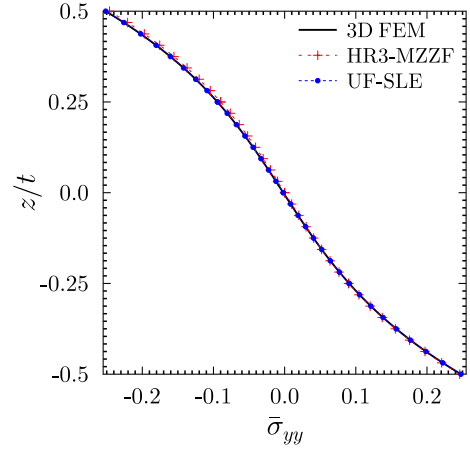
4. Conclusions

Previous studies [39, 44, 49] highlighted the ability of the Unified Formulation, based on Serendipity Lagrange expansions (UF-SLE), in capturing localised three-dimensional (3D) stress fields accurately in isotropic, laminated composite and sandwich structures. In this work, the UF-SLE model is extended for analysing Variable Angle Tow (VAT) structures and is benchmarked against 3D Finite Element (FE) solutions and an equivalent single-layer mixed formulation based on the Hellinger-Reissner principle. The hierarchical nature of the present approach allows the fidelity of the model to be tuned, such that low-fidelity and high-fidelity models can be used concurrently to assess global response and 3D stresses, even when highly localised. Moreover, this feature offers computational benefits over 3D FE models while maintaining a similar level of accuracy.

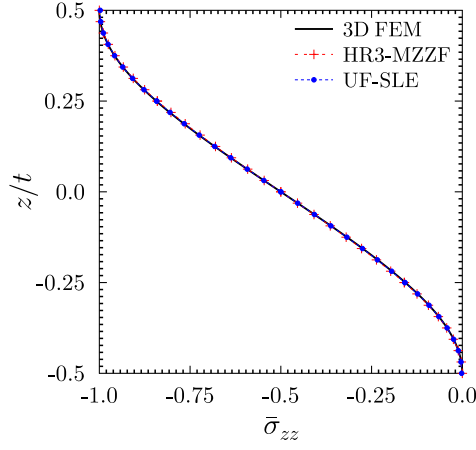
The present study also highlights the subtle implications of the commonly used linear fibre-orientation expression for VAT laminates, as given by Eq. (10). The presence of an absolute function in the expression introduces a mathematical singularity within the domain of a continuous fibre distribution, which leads to localised stress concentrations in the transverse stresses, and which may have implications for failure prediction and design considerations. This condition is often overlooked by researchers when modelling VAT composites. For instance, in the case of the HR3-MZZF model [36], a Differential Quadrature method (DQM) was employed to model the beam structure using a single continuous domain. This modelling technique yields inaccurate transverse shear stress distributions at the beam's mid-span where the singularity, and hence a mathematical boundary, is present. This inaccuracy in the transverse shear stress calculation was further amplified in the computation of the transverse normal stress. In contrast, the present approach uses a finite element discretisation along the beam direction, and therefore, separates the domain at the point of mathematical singularity. Hence, such an approach is also required for the DQM-based HR model and can readily be implemented using an element-based domain decomposition such as the differential quadrature-based FE method [50].



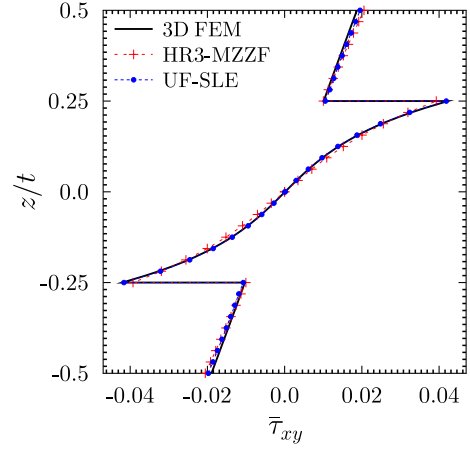
(a) Lateral normal stress, $\bar{\sigma}_{xx}(a/2, b/2, z)$



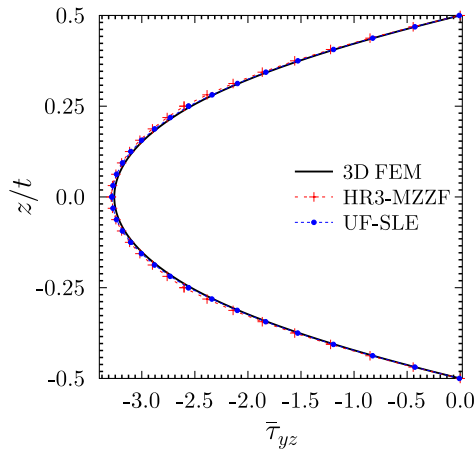
(b) Axial normal stress, $\bar{\sigma}_{yy}(a/2, b/2, z)$



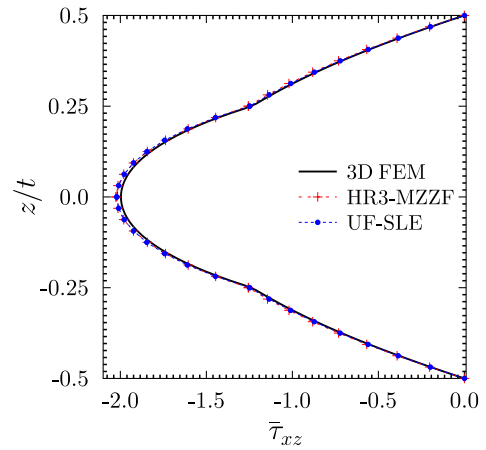
(c) Transverse normal stress, $\bar{\sigma}_{zz}(a/2, b/2, z)$



(d) In-plane shear stress, $\bar{\tau}_{xy}(a/4, b/4, z)$

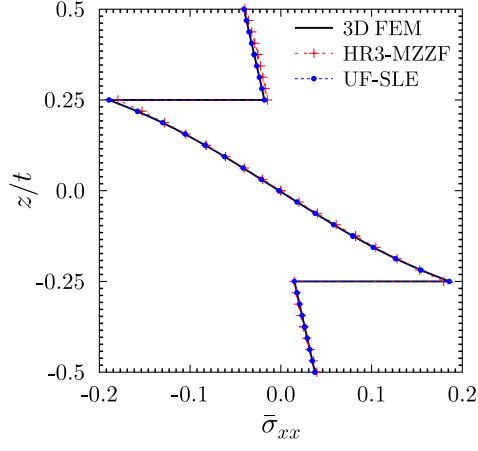


(e) Transverse shear stress, $\bar{\tau}_{yz}(a/2, b/4, z)$

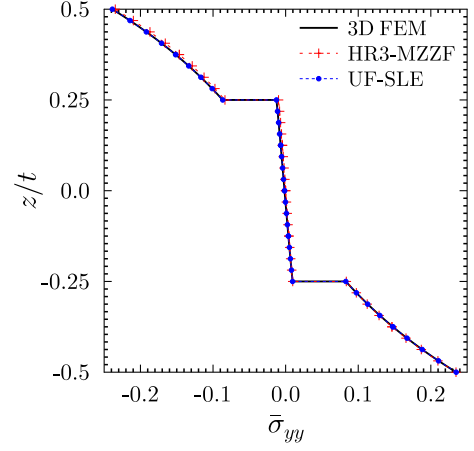


(f) Transverse shear stress, $\bar{\tau}_{xz}(a/4, b/2, z)$

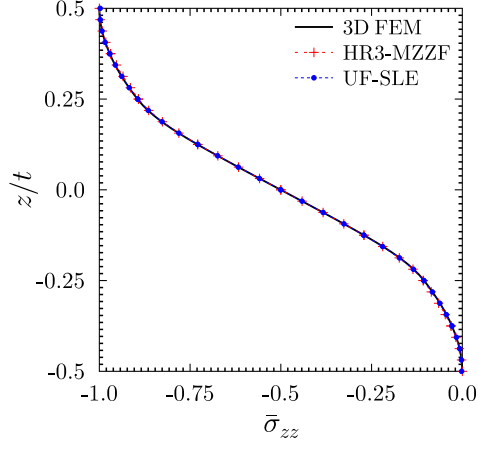
Figure 21: Through-thickness distribution of the 3D stress field at different planar locations for VAT plate K.



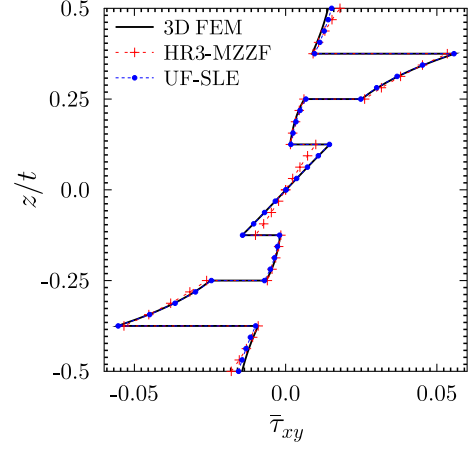
(a) Lateral normal stress, $\bar{\sigma}_{xx}(a/2, b/2, z)$



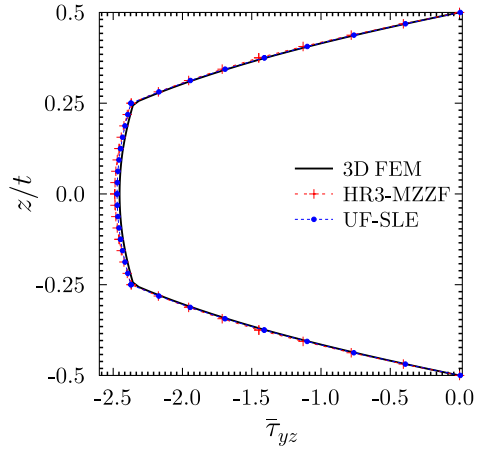
(b) Axial normal stress, $\bar{\sigma}_{yy}(a/2, b/2, z)$



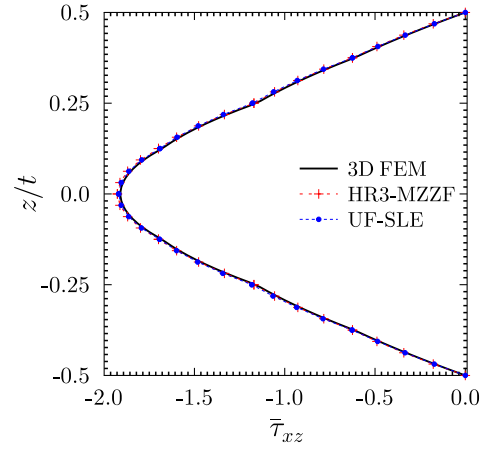
(c) Transverse normal stress, $\bar{\sigma}_{zz}(a/2, b/2, z)$



(d) In-plane shear stress, $\bar{\tau}_{xy}(a/4, b/4, z)$

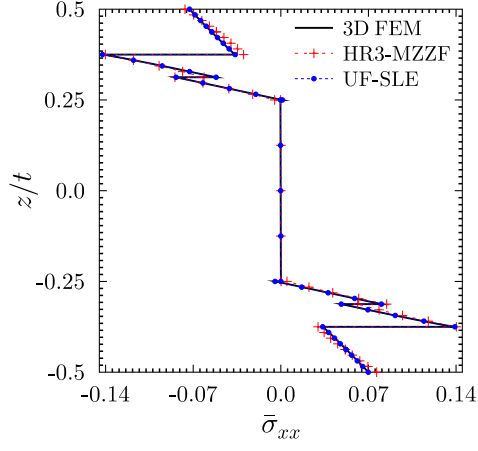


(e) Transverse shear stress, $\bar{\tau}_{yz}(a/2, b/4, z)$

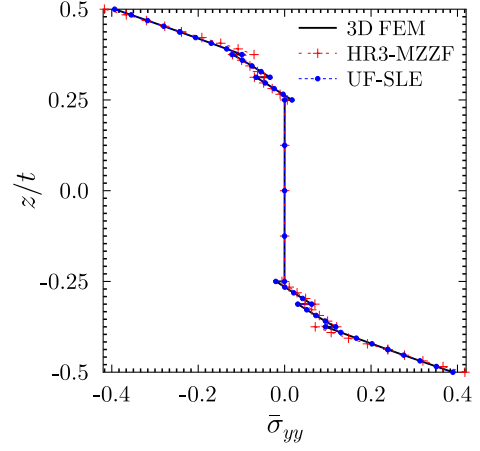


(f) Transverse shear stress, $\bar{\tau}_{xz}(a/4, b/2, z)$

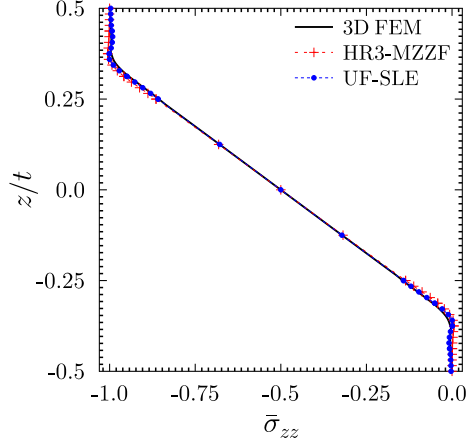
Figure 22: Through-thickness distribution of the 3D stress field at different planar locations for VAT plate L.



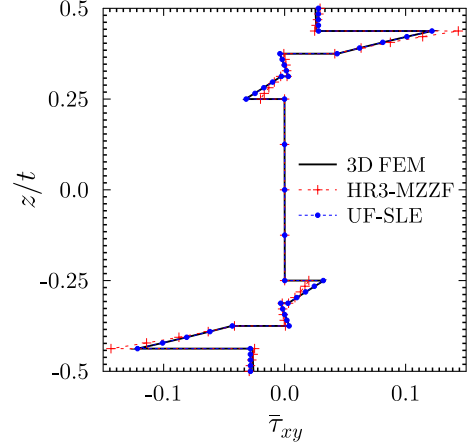
(a) Lateral normal stress, $\bar{\sigma}_{xx}(a/2, b/2, z)$



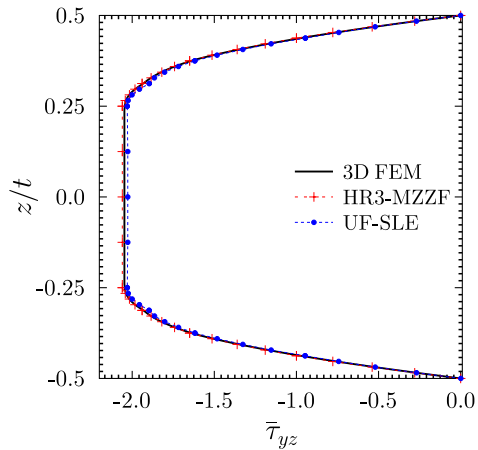
(b) Axial normal stress, $\bar{\sigma}_{yy}(a/2, b/2, z)$



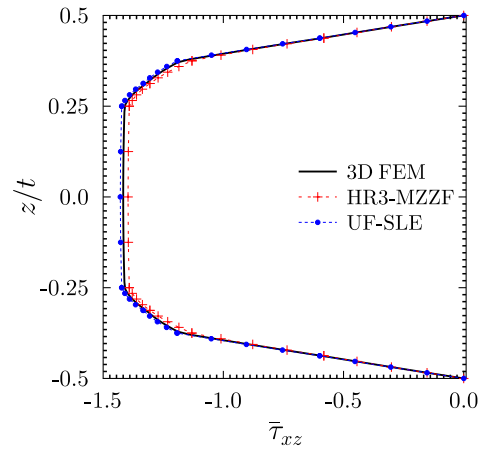
(c) Transverse normal stress, $\bar{\sigma}_{zz}(a/2, b/2, z)$



(d) In-plane shear stress, $\bar{\tau}_{xy}(a/4, b/4, z)$



(e) Transverse shear stress, $\bar{\tau}_{yz}(a/2, b/4, z)$



(f) Transverse shear stress, $\bar{\tau}_{xz}(a/4, b/2, z)$

Figure 23: Through-thickness distribution of the 3D stress field at different planar locations for VAT plate M.

Acknowledgements

This research has been developed in the framework of the FULLCOMP project, supported by the H2020 Marie Skłodowska-Curie European Training Network [Grant No. 642121]. Alberto Pirrera is funded by the EPSRC [Grant No. EP/M013170/1]. Rainer Groh is supported by the Royal Academy of Engineering under the Research Fellowship scheme [Grant No. RF\201718\17178]. Paul M. Weaver would like to acknowledge the support of the Royal Society for the Royal Society Wolfson Merit and the Science Foundation Ireland for the award of a Research Professor grant (Varicomp: 15/RP/2773).

Appendix A: Fundamental Nucleus

The fundamental nucleus $\mathbf{K}^{\tau sij}$ is a (3×3) matrix and the explicit expression for its components is given by

$$\begin{aligned}
K_{xx}^{\tau sij} = & \int_A F_\tau F_s dx dz \int_l \bar{C}(6,6) N_{i,y} N_{j,y} dy + \int_A F_{\tau,z} F_{s,z} dx dz \int_l \bar{C}(5,5) N_i N_j dy \\
& + \int_A F_\tau F_{s,z} dx dz \int_l \bar{C}(5,6) N_{i,y} N_j dy + \int_A F_{\tau,z} F_s dx dz \int_l \bar{C}(5,6) N_i N_{j,y} dy \\
& + \int_A F_{\tau,z} F_{s,x} dx dz \int_l \bar{C}(1,5) N_i N_j dy + \int_A F_{\tau,x} F_{s,z} dx dz \int_l \bar{C}(1,5) N_i N_j dy \\
& + \int_A F_\tau F_{s,x} dx dz \int_l \bar{C}(1,6) N_{i,y} N_j dy + \int_A F_{\tau,x} F_s dx dz \int_l \bar{C}(1,6) N_i N_{j,y} dy \\
& + \int_A F_{\tau,x} F_{s,x} dx dz \int_l \bar{C}(1,1) N_i N_j dy,
\end{aligned} \tag{18}$$

$$\begin{aligned}
K_{xy}^{\tau sij} = & \int_A F_{\tau,z} F_s dx dz \int_l \bar{C}(4,6) N_i N_{j,y} dy + \int_A F_{\tau,x} F_s dx dz \int_l \bar{C}(6,6) N_i N_{j,y} dy \\
& + \int_A F_\tau F_{s,z} dx dz \int_l \bar{C}(2,5) N_{i,y} N_j dy + \int_A F_\tau F_{s,x} dx dz \int_l \bar{C}(1,2) N_{i,y} N_j dy \\
& + \int_A F_{\tau,z} F_{s,z} dx dz \int_l \bar{C}(4,5) N_i N_j dy + \int_A F_{\tau,z} F_{s,x} dx dz \int_l \bar{C}(1,4) N_i N_j dy \\
& + \int_A F_{\tau,x} F_{s,z} dx dz \int_l \bar{C}(5,6) N_i N_j dy + \int_A F_\tau F_s dx dz \int_l \bar{C}(2,6) N_{i,y} N_{j,y} dy \\
& + \int_A F_{\tau,x} F_{s,x} dx dz \int_l \bar{C}(1,6) N_i N_j dy,
\end{aligned} \tag{19}$$

$$\begin{aligned}
K_{xz}^{\tau sij} = & \int_A F_\tau F_s dx dz \int_l \bar{C}(4,6) N_{i,y} N_{j,y} dy + \int_A F_{\tau,z} F_s dx dz \int_l \bar{C}(3,6) N_i N_{j,y} dy \\
& + \int_A F_{\tau,x} F_s dx dz \int_l \bar{C}(5,6) N_i N_{j,y} dy + \int_A F_\tau F_{s,z} dx dz \int_l \bar{C}(4,5) N_{i,y} N_j dy \\
& + \int_A F_\tau F_{s,x} dx dz \int_l \bar{C}(1,4) N_{i,y} N_j dy + \int_A F_{\tau,z} F_{s,z} dx dz \int_l \bar{C}(3,5) N_i N_j dy \\
& + \int_A F_{\tau,z} F_{s,x} dx dz \int_l \bar{C}(1,3) N_i N_j dy + \int_A F_{\tau,x} F_{s,z} dx dz \int_l \bar{C}(5,5) N_i N_j dy \\
& + \int_A F_{\tau,x} F_{s,x} dx dz \int_l \bar{C}(1,5) N_i N_j dy,
\end{aligned} \tag{20}$$

$$\begin{aligned}
K_{yx}^{\tau sij} = & \int_A F_{\tau,z} F_s dx dz \int_l \bar{C}(2,5) N_i N_{j,y} dy + \int_A F_{\tau,x} F_s dx dz \int_l \bar{C}(1,2) N_i N_{j,y} dy \\
& + \int_A F_{\tau} F_{s,z} dx dz \int_l \bar{C}(4,6) N_{i,y} N_j dy + \int_A F_{\tau} F_{s,x} dx dz \int_l \bar{C}(6,6) N_{i,y} N_j dy \\
& + \int_A F_{\tau,z} F_{s,z} dx dz \int_l \bar{C}(4,5) N_i N_j dy + \int_A F_{\tau,z} F_{s,x} dx dz \int_l \bar{C}(5,6) N_i N_j dy \\
& + \int_A F_{\tau,x} F_{s,z} dx dz \int_l \bar{C}(1,4) N_i N_j dy + \int_A F_{\tau} F_s dx dz \int_l \bar{C}(2,6) N_{i,y} N_{j,y} dy \\
& + \int_A F_{\tau,x} F_{s,x} dx dz \int_l \bar{C}(1,6) N_i N_j dy,
\end{aligned} \tag{21}$$

$$\begin{aligned}
K_{yy}^{\tau sij} = & \int_A F_{\tau} F_s dx dz \int_l \bar{C}(2,2) N_{i,y} N_{j,y} dy + \int_A F_{\tau,z} F_s dx dz \int_l \bar{C}(2,4) N_i N_{j,y} dy \\
& + \int_A F_{\tau} F_{s,z} dx dz \int_l \bar{C}(2,4) N_{i,y} N_j dy + \int_A F_{\tau,z} F_{s,z} dx dz \int_l \bar{C}(4,4) N_i N_j dy \\
& + \int_A F_{\tau,z} F_{s,x} dx dz \int_l \bar{C}(4,6) N_i N_j dy + \int_A F_{\tau,x} F_{s,z} dx dz \int_l \bar{C}(4,6) N_i N_j dy \\
& + \int_A F_{\tau,x} F_{s,x} dx dz \int_l \bar{C}(6,6) N_i N_j dy + \int_A F_{\tau,x} F_s dx dz \int_l \bar{C}(2,6) N_i N_{j,y} dy \\
& + \int_A F_{\tau} F_{s,x} dx dz \int_l \bar{C}(2,6) N_{i,y} N_j dy,
\end{aligned} \tag{22}$$

$$\begin{aligned}
K_{yz}^{\tau sij} = & \int_A F_{\tau} F_s dx dz \int_l \bar{C}(2,4) N_{i,y} N_{j,y} dy + \int_A F_{\tau,z} F_s dx dz \int_l \bar{C}(2,3) N_i N_{j,y} dy \\
& + \int_A F_{\tau,x} F_s dx dz \int_l \bar{C}(2,5) N_i N_{j,y} dy + \int_A F_{\tau} F_{s,z} dx dz \int_l \bar{C}(4,4) N_{i,y} N_j dy \\
& + \int_A F_{\tau} F_{s,x} dx dz \int_l \bar{C}(4,6) N_{i,y} N_j dy + \int_A F_{\tau,z} F_{s,z} dx dz \int_l \bar{C}(3,4) N_i N_j dy \\
& + \int_A F_{\tau,z} F_{s,x} dx dz \int_l \bar{C}(3,6) N_i N_j dy + \int_A F_{\tau,x} F_{s,z} dx dz \int_l \bar{C}(4,5) N_i N_j dy \\
& + \int_A F_{\tau,x} F_{s,x} dx dz \int_l \bar{C}(5,6) N_i N_j dy,
\end{aligned} \tag{23}$$

$$\begin{aligned}
K_{zx}^{\tau sij} = & \int_A F_{\tau} F_s dx dz \int_l \bar{C}(4,6) N_{i,y} N_{j,y} dy + \int_A F_{\tau,z} F_s dx dz \int_l \bar{C}(4,5) N_i N_{j,y} dy \\
& + \int_A F_{\tau,x} F_s dx dz \int_l \bar{C}(1,4) N_i N_{j,y} dy + \int_A F_{\tau} F_{s,z} dx dz \int_l \bar{C}(3,6) N_{i,y} N_j dy \\
& + \int_A F_{\tau} F_{s,x} dx dz \int_l \bar{C}(5,6) N_{i,y} N_j dy + \int_A F_{\tau,z} F_{s,z} dx dz \int_l \bar{C}(3,5) N_i N_j dy \\
& + \int_A F_{\tau,z} F_{s,x} dx dz \int_l \bar{C}(5,5) N_i N_j dy + \int_A F_{\tau,x} F_{s,z} dx dz \int_l \bar{C}(1,3) N_i N_j dy \\
& + \int_A F_{\tau,x} F_{s,x} dx dz \int_l \bar{C}(1,5) N_i N_j dy,
\end{aligned} \tag{24}$$

$$\begin{aligned}
K_{zy}^{\tau sij} = & \int_A F_\tau F_s dx dz \int_l \bar{C}(2,4) N_{i,y} N_{j,y} dy + \int_A F_{\tau,z} F_s dx dz \int_l \bar{C}(4,4) N_i N_{j,y} dy \\
& + \int_A F_{\tau,x} F_s dx dz \int_l \bar{C}(4,6) N_i N_{j,y} dy + \int_A F_\tau F_{s,z} dx dz \int_l \bar{C}(2,3) N_{i,y} N_j dy \\
& + \int_A F_\tau F_{s,x} dx dz \int_l \bar{C}(2,5) N_{i,y} N_j dy + \int_A F_{\tau,z} F_{s,z} dx dz \int_l \bar{C}(3,4) N_i N_j dy \\
& + \int_A F_{\tau,z} F_{s,x} dx dz \int_l \bar{C}(4,5) N_i N_j dy + \int_A F_{\tau,x} F_{s,z} dx dz \int_l \bar{C}(3,6) N_i N_j dy \\
& + \int_A F_{\tau,x} F_{s,x} dx dz \int_l \bar{C}(5,6) N_i N_j dy,
\end{aligned} \tag{25}$$

$$\begin{aligned}
K_{zz}^{\tau sij} = & \int_A F_\tau F_s dx dz \int_l \bar{C}(4,4) N_{i,y} N_{j,y} dy + \int_A F_{\tau,z} F_s dx dz \int_l \bar{C}(3,4) N_i N_{j,y} dy \\
& + \int_A F_{\tau,x} F_s dx dz \int_l \bar{C}(4,4) N_i N_{j,y} dy + \int_A F_\tau F_{s,z} dx dz \int_l \bar{C}(3,4) N_{i,y} N_j dy \\
& + \int_A F_\tau F_{s,x} dx dz \int_l \bar{C}(4,5) N_{i,y} N_j dy + \int_A F_{\tau,z} F_{s,z} dx dz \int_l \bar{C}(3,3) N_i N_j dy \\
& + \int_A F_{\tau,z} F_{s,x} dx dz \int_l \bar{C}(3,5) N_i N_j dy + \int_A F_{\tau,x} F_{s,z} dx dz \int_l \bar{C}(3,5) N_i N_j dy \\
& + \int_A F_{\tau,x} F_{s,x} dx dz \int_l \bar{C}(5,5) N_i N_j dy,
\end{aligned} \tag{26}$$

Appendix B: Hooke's Law for Plane-Strain

For the case of plane-strain, where the strains in the x -direction are considered to be negligible, $\varepsilon_{xx} = \gamma_{xz} = \gamma_{xy} = 0$, the stress-strain stiffness relationship for a lamina becomes

$$\begin{Bmatrix} \sigma_{xx} \\ \sigma_{yy} \\ \sigma_{zz} \\ \tau_{yz} \\ \tau_{xz} \\ \tau_{xy} \end{Bmatrix} = \begin{bmatrix} \bar{C}_{11} & \bar{C}_{12} & \bar{C}_{13} & \bar{C}_{14} & \bar{C}_{15} & \bar{C}_{16} \\ \bar{C}_{21} & \bar{C}_{22} & \bar{C}_{23} & \bar{C}_{24} & \bar{C}_{25} & \bar{C}_{26} \\ \bar{C}_{31} & \bar{C}_{32} & \bar{C}_{33} & \bar{C}_{34} & \bar{C}_{35} & \bar{C}_{36} \\ \bar{C}_{41} & \bar{C}_{42} & \bar{C}_{43} & \bar{C}_{44} & \bar{C}_{45} & \bar{C}_{46} \\ \bar{C}_{51} & \bar{C}_{52} & \bar{C}_{53} & \bar{C}_{54} & \bar{C}_{55} & \bar{C}_{56} \\ \bar{C}_{61} & \bar{C}_{62} & \bar{C}_{63} & \bar{C}_{64} & \bar{C}_{65} & \bar{C}_{66} \end{bmatrix} \begin{Bmatrix} 0 \\ \varepsilon_{yy} \\ \varepsilon_{zz} \\ \gamma_{yz} \\ 0 \\ 0 \end{Bmatrix}. \tag{27}$$

The three zero strain entries in the strain vector indicate that their associated columns in the stiffness matrix (*i.e.* columns 1, 5, and 6) can be ignored. If the rows associated with the stress components with x -subscripts are also ignored, then, the stiffness matrix reduces to a simple 3×3 matrix, as given by

$$\begin{Bmatrix} \sigma_{yy} \\ \sigma_{zz} \\ \tau_{yz} \end{Bmatrix} = \begin{bmatrix} \bar{C}_{22} & \bar{C}_{23} & \bar{C}_{24} \\ \bar{C}_{32} & \bar{C}_{33} & \bar{C}_{34} \\ \bar{C}_{42} & \bar{C}_{43} & \bar{C}_{44} \end{bmatrix} \begin{Bmatrix} \varepsilon_{yy} \\ \varepsilon_{zz} \\ \gamma_{yz} \end{Bmatrix}. \tag{28}$$

In order to model the plane-strain behavior within the Unified Formulation framework, we use the following material stiffness matrix

$$\begin{Bmatrix} \sigma_{xx} \\ \sigma_{yy} \\ \sigma_{zz} \\ \tau_{yz} \\ \tau_{xz} \\ \tau_{xy} \end{Bmatrix} = \begin{bmatrix} \bar{C}_{11} & 0 & 0 & 0 & 0 & 0 \\ 0 & \bar{C}_{22} & \bar{C}_{23} & \bar{C}_{24} & 0 & 0 \\ 0 & \bar{C}_{32} & \bar{C}_{33} & \bar{C}_{34} & 0 & 0 \\ 0 & \bar{C}_{42} & \bar{C}_{43} & \bar{C}_{44} & 0 & 0 \\ 0 & 0 & 0 & 0 & \bar{C}_{55} & 0 \\ 0 & 0 & 0 & 0 & 0 & \bar{C}_{66} \end{bmatrix} \begin{Bmatrix} \varepsilon_{xx} \\ \varepsilon_{yy} \\ \varepsilon_{zz} \\ \gamma_{yz} \\ \gamma_{xz} \\ \gamma_{xy} \end{Bmatrix}. \tag{29}$$

References

References

- [1] Z. Gürdal, R. Olmedo, In-plane response of laminates with spatially varying fiber orientations: variable stiffness concept, *AIAA Journal* 31(4) (1993) 751 – 758.
- [2] P. Ribeiro, H. Akhavan, A. Teter, J. Warmański, A review on the mechanical behaviour of curvilinear fibre composite laminated panels, *Journal of Composite Materials* 48 (2014) 2761 – 2777.
- [3] L. Bittrich, A. Spickenheuer, J. H. S. Almeida, S. Müller, L. Kroll, G. Heinrich, Optimizing Variable-Axial Fiber-Reinforced Composite Laminates: The Direct Fiber Path Optimization Concept, *Mathematical Problems in Engineering* 2019 (2019) 1 – 12.
- [4] A. A. G. Cooper, Trajectorial fiber reinforcement of composite structures, PhD thesis, Department of Mechanical and Aerospace Engineering, Washington University, 1972.
- [5] H. Ghiasi, K. Fayazbakhsh, D. Pasini, L. Lessard, Optimum stacking sequence design of composite materials Part II: Variable stiffness design, *Composite Structures* 93 (2010) 1 – 13.
- [6] M. Rouhi, H. Ghayoor, S. V. Hoa, M. Hojjati, P. M. Weaver, Stiffness tailoring of elliptical composite cylinders for axial buckling performance, *Composite Structures* 150 (2016) 115 – 123.
- [7] M. W. Hyer, H. Lee, The use of curvilinear fiber format to improve buckling resistance of composite plates with central circular holes, *Composite Structures* 18 (1991) 239 – 261.
- [8] S. Setoodeh, M. M. Abdalla, S. T. IJsselmuiden, Z. Gürdal, Design of variable-stiffness composite panels for maximum buckling load, *Composite Structures* 87 (2009) 109 – 117.
- [9] M. W. Hyer, R. F. Charette, Use of curvilinear fiber format in composite structure design, *AIAA Journal* 29 (1991) 1011 – 1015.
- [10] C. S. Lopes, Z. Gürdal, P. P. Camanho, Tailoring for strength of composite steered-fibre panels with cutouts, *Composites, Part A: Applied Science and Manufacturing* 41 (2010) 1760 – 1767.
- [11] Z. Gürdal, B. Tatting, C. Wu, Variable stiffness composite panels: Effects of stiffness variation on the in-plane and buckling response, *Composites, Part A: Applied Science and Manufacturing* 39 (2008) 911 – 922.
- [12] Z. Wu, P. M. Weaver, G. Raju, B. C. Kim, Buckling analysis and optimisation of variable angle tow composite plates, *Thin-Walled Structures* 60 (2012) 163 – 172.
- [13] Z. Wu, G. Raju, P. M. Weaver, Framework for the buckling optimization of variable angle tow composite plates, *AIAA Journal* 53 (2015) 1 – 17.
- [14] G. Raju, S. White, Z. Wu, Optimal postbuckling design of variable angle tow composites using lamination parameters, In *Proceedings of the 56th AIAA/ASME/ASCE/AHS/ASC Structures, Structural Dynamics and Materials Conference*, Kissimmee, Florida, USA.
- [15] P. Hao, C. Liu, X. Yuan, B. Wang, G. Li, T. Zhu, F. Niu, Buckling optimization of variable-stiffness composite panels based on flow field function, *Composite Structures* 181 (2017) 240 – 255.
- [16] Z. Stodiek, J. E. Cooper, P. M. Weaver, P. Kealy, Improved aeroelastic tailoring using tow-steered composites, *Composite Structures* 106 (2013) 703–715.
- [17] B. H. Coburn, Z. Wu, P. M. Weaver, Buckling analysis of stiffened variable angle tow panels, *Composite Structures* 111 (2014) 259 – 270.
- [18] S. Scott, M. Capuzzi, D. Langston, E. Bossanyi, G. McCann, P. M. Weaver, A. Pirrera, Effects of aeroelastic tailoring on performance characteristics of wind turbine systems, *Renewable Energy* 114 (2017) 887–903.
- [19] M. M. Abdalla, S. Setoodeh, Z. Gürdal, Design of variable stiffness composite panels for maximum fundamental frequency using lamination parameters, *Composite Structures* 81 (2007) 283 – 291.
- [20] A. W. Blom, S. Setoodeh, J. M. A. M. Hol, Z. Gürdal, Design of variable-stiffness conical shells for maximum fundamental eigen frequency, *Composite Structures* 86 (2008) 870 – 878.
- [21] H. Akhavan, P. Ribeiro, Natural modes of vibration of variable stiffness composite laminates with curvilinear fibers, *Composite Structures* 93 (2011) 3040 – 3047.
- [22] P. Ribeiro, Non-linear free periodic vibrations of variable stiffness composite laminated plates, *Nonlinear Dynamics* 70 (2012) 1535 – 1548.
- [23] Z. Wu, P. M. Weaver, G. Raju, Postbuckling optimisation of variable angle tow composite plates, *Composite Structures* 103 (2013) 34 – 42.
- [24] Z. Xin, Y. Duan, W. Xu, T. Zhang, B. Wang, Review of the mechanical performance of variable stiffness design fiber-reinforced composites, *Science and Engineering of Composite Materials* 25(3) (2016) 425 – 437.
- [25] R. M. J. Groh, P. M. Weaver, Deleterious localized stress fields: the effects of boundaries and stiffness tailoring in anisotropic laminated plates, *Proceedings of the Royal Society A, Mathematical, Physical and Engineering Sciences* 472 (2194) (2016) 1 – 22.
- [26] A. H. Akbarzadeh, M. A. Nik, D. Pasini, The role of shear deformation in laminated plates with curvilinear fiber paths and embedded defects, *Composite Structures* 118 (2014) 217 – 227.
- [27] H. Akhavan, P. Ribeiro, Non-linear vibrations of variable stiffness composite laminated plates, *Composite Structures* 94 (2012) 2424 – 2432.
- [28] H. Akhavan, P. Ribeiro, M. F. S. F. de Moura, Large deflection and stresses in variable stiffness composite laminates with curvilinear fibre, *International Journal of Mechanical Sciences* 73 (2013) 14 – 26.
- [29] J. Díaz, C. Fagiano, M. M. Abdalla, Z. Gürdal, S. Hernández, A study of interlaminar stresses in variable stiffness plates, *Composite Structures* 94 (2012) 1192 – 1199.

- [30] R. M. J. Groh, P. M. Weaver, Static inconsistencies in certain axiomatic higher-order shear deformation theories for beams, plates and shells, *Composite Structures* 120 (2015) 231 – 245.
- [31] A. Soriano, J. Díaz, Failure analysis of variable stiffness composite plates using continuum damage mechanics models, *Composite Structures* 184 (2018) 1071 – 1080.
- [32] L. Demasi, G. Biagini, F. Vannucci, E. Santarpia, R. Cavallaro, Equivalent single layer, zig-zag, and layer wise theories for variable angle tow composites based on the generalized unified formulation, *Composite Structures* 177 (2017) 54 – 79.
- [33] L. Demasi, Hierarchy plate theories for thick and thin composite plates: The generalized unified formulation, *Composite Structures* 84 (2008) 256–270.
- [34] F. Tornabene, N. Fantuzzi, M. Baccocchi, E. Viola, Higher-order theories for the free vibrations of doubly-curved laminated panels with curvilinear reinforcing fibers by means of a local version of the gdq method, *Composites Part B: Engineering* 81 (2015) 196 – 230.
- [35] F. Tornabene, M. Baccocchi, Effect of Curvilinear Reinforcing Fibers on the Linear Static Behavior of Soft-Core Sandwich Structures, *Journal of Composites Science* 2(14) (2018) 1 – 43.
- [36] R. M. J. Groh, Non-classical effects in straight-fibre and tow-steered composite beams and plates, PhD thesis, Department of Aerospace Engineering, University of Bristol, 2015.
- [37] R. M. J. Groh, P. M. Weaver, A computationally efficient 2D model for inherently equilibrated 3D stress predictions in heterogeneous laminated plates. Part I: Model formulation, *Composite Structures* 156 (2016) 171–185.
- [38] G. Raju, Z. Wu, B. C. Kim, P. M. Weaver, Prebuckling and buckling analysis of variable angle tow plates with general boundary conditions, *Composite Structures* 94 (2012) 2961 – 2970.
- [39] M. Patni, S. Minera, R. M. J. Groh, A. Pirrera, P. M. Weaver, Three-dimensional stress analysis for laminated composite and sandwich structures, *Composites Part B: Engineering* 155 (2018) 299–328.
- [40] E. Carrera, M. Cinefra, M. Petrolo, E. Zappino, *Finite Element Analysis of Structures through Unified Formulation*, Wiley, Politecnico di Torino, Italy, 2014.
- [41] A. Catapano, G. Giunta, S. Belouettar, E. Carrera, Static analysis of laminated beams via a unified formulation, *Composite Structures* 94 (2011) 75–83.
- [42] E. Carrera, G. Giunta, Refined beam theories based on a unified formulation, *International Journal of Applied Mechanics* 02 (2010) 117–143.
- [43] E. Carrera, G. Giunta, M. Petrolo, *A Modern and Compact Way to Formulate Classical and Advanced Beam Theories*, Saxe-Coburg Publications, United Kingdom, 2010.
- [44] S. Minera, M. Patni, E. Carrera, M. Petrolo, P. M. Weaver, A. Pirrera, Three-dimensional stress analysis for beam-like structures using serendipity lagrange shape functions, *International Journal of Solids and Structures* 141-142 (2018) 279 – 296.
- [45] R. M. J. Groh, P. M. Weaver, S. White, G. Raju, Z. Wu, A 2D equivalent single-layer formulation for the effect of transverse shear on laminated plates with curvilinear fibres, *Composite Structures* 100 (2013) 464–478.
- [46] H. Murakami, Laminated composite plate theory with improved in-plane responses, *Journal of Applied Mechanics* 53 (1986) 661 – 666. doi:10.1115/1.3171828.
- [47] A. Tessler, Refined zigzag theory for homogeneous, laminated composite, and sandwich beams derived from Reissner’s mixed variational principle, *Advances in the Mechanics of Composite and Sandwich Structures* 50 (10) (2015) 2621–2648.
- [48] J. N. Reddy, *Mechanics of Laminated Composite Plates and Shells. Theory and Analysis*, Second Edition, CRC Press, 2004.
- [49] M. Patni, S. Minera, P. M. Weaver, A. Pirrera, A computationally efficient model for three-dimensional stress analysis of stiffened curved panels, *Proceedings of the International Conference on Composite Materials and Structures (ICCMS)*, Hyderabad, India (December, 2017) 1–12.
- [50] F. Tornabene, N. Fantuzzi, F. Ubertini, E. Viola, Strong formulation finite element method based on differential quadrature: A survey, *Applied Mechanics Reviews* 67 (2015) 020801.